MULTIPHASE TITANATE-BASED CERAMIC WASTE FORMS: CERIUM INCORPORATION IN ZIRCONOLITE AND PYROCHLORE AND RADIATION STABILITY

BY

BRAEDEN MATTHEW CLARK

A THESIS

SUBMITTED TO THE FACULTY OF

ALFRED UNIVERSITY

IN PARTIAL FULFILLMENT OF THE REQUIREMENTS
FOR THE DEGREE OF

DOCTOR OF PHILOSOPHY

IN

CERAMIC ENGINEERING

ALFRED, NEW YORK

AUGUST, 2018

MULTIPHASE TITANATE-BASED CERAMIC WASTE FORMS: CERIUM INCORPORATION IN ZIRCONOLITE AND PYROCHLORE AND RADIATION STABILITY

BY

BRAEDEN MATTHEW CLARK

B.S. ALFRED UNIVERSITY, ALFRED, NY (2012)

SIGNATURE OF AUTHOR _____

APPROVED BY _____
S. K. SUNDARAM, ADVISOR

_____
SCOTT T. MISTURE, ADVISORY COMMITTEE

_____
YIQUAN WU, ADVISORY COMMITTEE

_____
ALASTAIR N. CORMACK, ADVISORY COMMITTEE

_____
WILLIAM M. CARTY, CHAIR, ORAL THESIS DEFENSE

ACCEPTED BY _____
ALASTAIR N. CORMACK, INTERIM DEAN
KAZUO INAMORI SCHOOL OF ENGINEERING

ACCEPTED BY _____
W. RICHARD STEPHENS JR.
PROVOST AND VP FOR ACADEMIC AFFAIRS
ALFRED UNIVERSITY

ACKNOWLEDGMENTS

This work was supported by the Department of Energy (DOE) Nuclear Energy University Program (NEUP) grant NEUP_12-3809 and a fellowship from the NEUP. I would like to sincerely thank my advisor, Dr. S.K. Sundaram, as well as my thesis committee members, Dr. S.T. Misture, Dr. Y. Wu, and Dr. A.N. Cormack, for their support and guidance throughout these past six years.

My work utilized facilities in national laboratories and other institutions. Radiation damage work was performed in collaboration with the Environmental Molecular Sciences Laboratory (EMSL) at Pacific Northwest National Laboratory (PNNL), the Ion Beam Materials Laboratory (IBML) at Los Alamos National Laboratory (LANL) and the Ion Beam Laboratory (IBL) at the University at Albany (UA). Many thanks are extended to the researchers that aided this work, in particular, Dr. V. Shuttha (EMSL), Dr. M. Tang (LANL), and Dr. M Huang (UA). Chemical durability work was performed at Savannah River National Laboratory (SRNL) and the guidance and assistance of Dr. J.W. Amoroso, Dr. J.C. Marra, and Mrs. P. Workman is greatly appreciated. Some work is based upon research conducted at the Cornell High Energy Synchrotron Source (CHESS) which is supported by the National Science Foundation and the National Institutes of Health/National Institute of General Medical Sciences under NSF award DMR-1332208, in particular, the help of Dr. R. Huang is greatly appreciated. Additional work made use of the electron microscopy facility of the Cornell Center for Materials Research (CCMR) with support from the National Science Foundation Materials Research Science and Engineering Centers (MRSEC) program (DMR 1120296).

The staff at Alfred University has been instrumental in helping me complete this work, namely Gerry Wynick and Swavek Zdzieszynski for all their guidance on the laboratory instruments. Katie Decker and Tiffany Horton deserve the utmost thanks for all the work that they do and for helping me with so much over the years!

My family and friends have kept me sane and motivated throughout this degree. I could not have done this without all of you. I love you.

Disclaimer

Most of these results have been already been published in the open literature. In some cases, several paragraphs are reproduced verbatim in this thesis.

Section III. Phase Assemblage and Microstructure of Multiphase Ceramic Waste Forms
B. M. Clark, P. Tumurugoti, S. K. Sundaram, J. W. Amoroso, J. C. Marra, and K. S. Brinkman, "Microstructures of Melt-Processed and Spark Plasma Sintered Ceramic Waste Forms," *Metall. Mater. Trans. E*, **1** [4] 341-8 (2014).

Section IV. Radiation Damage of Hollandite in Multiphase Ceramic Waste Forms
B. M. Clark, P. Tumurgoti, S. K. Sundaram, J. W. Amoroso, J. C. Marra, V. Shutthanandan, and M. Tang, "Radiation Damage of Hollandite in Multiphase Ceramic Waste Forms," *J. Nucl. Mater.,* **494** 61-6 (2017).

Section V. Cerium Substitution and Spark Plasma Sintering of Zirconolite ($CaZrTi_2O_7$) and Pyrochlore ($Nd_2Ti_2O_7$)
B. M. Clark, S. K. Sundaram, and S. T. Misture, "Polymorphic Transitions in Cerium-Substituted Zirconolite ($CaZrTi_2O_7$)," *Scientific Reports,* **7** [1] 5920 (2017).

TABLE OF CONTENTS

LIST OF TABLES

LIST OF FIGURES

ABSTRACT

This thesis aims at developing ceramic waste forms as a potential replacement for the conventional glass waste forms for safe immobilization and disposal of nuclear wastes from legacy weapons programs as well as commercial power production. The body of work consists of two parts. The first part focused on fabrication and characterization of multiphase waste forms containing hollandite as the major phase with perovskite, pyrochlore, and zirconolite as secondary phases. The second part focuses on single phase pyrochlores and zirconolites for cerium (Ce) incorporation.

Part I: Multiphase waste forms:

Compositions of simulated multiphase waste forms were developed at Savannah River National Laboratory (SRNL) and processed at Alfred University using melt-processing and spark plasma sintering (SPS). The resulting multiphase waste forms contained a majority of hollandite along with perovskite, pyrochlore, and zirconolite phases as determined by X-ray diffraction (XRD) and energy dispersive spectroscopy (EDS). Cesium (Cs) incorporation into the hollandite phase is more prevalent in melt-processed sample, requiring further optimization of the SPS process.

Radiation damage resistance is a vital performance requirement for waste forms. This was simulated in these multiphase ceramics by bombarding the samples with Au^{3+} and He^{+} ions. Heavy ions (Au^{3+}) initiated ballistic processes that caused all phases in the affected volumes to amorphize. Regardless of the processing method, the amorphization behavior remained the same in all samples bombarded with Au^{3+} ions. The ion penetration depth was reduced in SPS-processed samples, attributed to the smaller grain sizes of these materials. Light ion (He^{+}) irradiation caused the breakdown of the hollandite phase, while the remaining phases appeared to be unaffected. This behavior was confirmed in single phase hollandite samples.

Part II: Single phase waste forms

High amounts of Ce can be incorporated into zirconolite and pyrochlore structures, up to 50 mol% for Zr in the case of zirconolite and 25 mol% for Nd in $Nd_2Ti_2O_7$ pyrochlore,

via solid state reaction. Perovskite is observed in small amounts in zirconolite materials (up to 7 wt%). With increasing Ce content, a transition from the 2M to 4M-zirconolite polymorph has been reported. The valence state of Ce will affect which atomic site that the Ce substitutes on. 2M-zirconolites contain trivalent Ce, which supports Ce substitution on both Ca and Zr sites. Both trivalent and tetravalent Ce are present in 4M-zirconolites, indicating greater partitioning onto the Zr site. All Ce substituted into pyrochlore materials is converted from tetravalent to trivalent during the reaction process to maintain charge neutrality of the structure.

Ce-substituted zirconolite and pyrochlore materials were consolidated using SPS. The reducing environment of the SPS causes 4M-zirconolite to convert to perovskite and 2M-zirconolite due to the reduction of Ce^{4+} to Ce^{3+} causing a redistribution of Ce onto the Ca and Zr sites of zirconolite and stabilizing perovskite. The original phase assemblage of the materials can be restored by a heat treatment in air post-sintering. $CaCeTi_2O_7$ forms as an intermediate phase up until 1300°C, and 4M-zirconolite begins at 1350°C. The transformation to 4M-zirconolite is slow, but complete conversion to the original phase assemblage is achieved with a 24h heat treatment in air. The sintering behavior of Ce-substituted pyrochlore is unaffected by Ce content in the material.

The integral waste form performance properties of radiation damage stability and chemical durability of Ce-substituted zirconolite and pyrochlore were simulated by implanting samples with He^{+} or Kr^{3+} with ion fluences equating to 0.5 dpa and Product Consistency Testing (PCT) and Materials Characterization Center (MCC-1) leach tests, respectively. Gracing-incidence x-ray diffraction (GIXRD) of the samples revealed that light ion (He^{+}) irradiation had very little effect on the materials, whereas heavy ion (Kr^{3+}) irradiation caused near complete amorphization of all materials tested, which corroborated well with the results from multiphase samples. No effect of Ce content on radiation damage behavior was seen. For zirconolite materials, Ce was only released during the PCT of $CaZr_{0.9}Ce_{0.1}Ti_2O_7$ indicating that the 4M-zirconolite polymorph is more chemically durable than 2M-zirconolite. Ce was released from $Nd_{1.5}Ce_{0.5}Ti_2O_7$ during both the PCT and MCC-1. During MCC-1 tests longer than 7 days, no Ce above the detectable limit of the ICP-AES was released. The Ce release values in these studies were comparable to those in similar tests performed previously in the literature.

I. INTRODUCTION

I.1. Nuclear Waste Generation

Reprocessing of spent nuclear fuel, defense weapon reprocessing, research activities (industrial, hospital, and university), industrial use of isotopes, and mining and refining of uranium ore are sources of the most dangerous classification of radioactive waste generation, or high level nuclear waste (HLW).[1] In certain cases, unprocessed spent nuclear fuel may need to be immobilized in nuclear waste forms if the recovery of the uranium (U) is not planned. Currently, the United States employs a once-through fuel cycle, meaning the fuel is used until it becomes economically unreasonable to generate energy.[2] The used nuclear fuel (UNF) is placed in a cooling and storage facility until eventual disposal in a geological repository. Due to the limited abundance of natural uranium and thorium, some countries have opted for the adoption of the closed nuclear fuel cycle. The closed nuclear fuel cycle utilizes the Plutonium-Uranium Extraction (PUREX) developed at Oak Ridge National Laboratory (ORNL) in 1950[3] to separate Pu and U from fission products (FPs) created from the burning of nuclear fuel. Tributyl phosphate is used as a solvent in the extraction process along with nitric acid as a salting agent, resulting in low losses (<0.1%) of plutonium and uranium.[3] The components of typical spent nuclear fuel are given in Table I-1.[4]

Table I-1. Components of Typical Spent Nuclear Fuel

Percentage after burnup	Component	Nature
95.6	Uranium	Recycled (closed) or disposed (open)
3	Short lived FPs	Decay in short time, not a significant disposal concern
0.3	Heat generating FPs	^{137}Cs and ^{90}Sr; cause heating of waste for a few centuries in long term storage
0.1	Long-lived FPs	Primarily I and Tc; present major challenges for storage, can be removed and/or transmuted
0.9	Plutonium	Separated and used as fuel (PUREX)
0.1	Long-lived minor actinides	Np, Am, Cm; can be separated and immobilized or immobilized along with FPs in multiphase waste forms

I.1.1 Energy Production

There are 449 operational nuclear reactors worldwide[5] that accounted for 10.9% of the world's energy production in 2012.[6] Many different nuclear power reactor designs are used worldwide.[7] To generate electricity, the fission process of ^{235}U is initiated by neutrons that have been slowed by a moderator (water or graphite). This process generates heat, which is used to produce steam that drives a turbine. Fuel rods are used as the fuel source for the U and the type of fuel rod changes contingent on the design of the reactor. In these different designs, UO_2 pellets are enclosed in different claddings such as stainless steel (advanced gas cooled reactors, AGR), zirconium alloy (pressurized water reactors, PWR, and boiling water reactors, BWR), or magnesium alloy (Magnox).[8]

To reprocess the spent fuel rods, the cladding is removed and the fuel is dissolved in nitric acid. Chemical solvent extraction (PUREX) is then performed to retrieve the unspent U as well as some Pu formed during the fuel burn-up process. Reprocessing the spent fuel rods generates waste consisting of fission products with atomic weights distributed around 46 (half of the atomic weight of U, such as Rb, Sr, Y, Zr, Nb, Mo, Tc, Ru, Rh, Pd, Cs, Ba, La, Ce, Pr, Nd, and Sm), cladding elements (Fe, Zr, and Mg), and transuranic elements formed by neutron capture (Np, Am, Cm, and Pu).[7,8]

I.1.2 Defense

Defense wastes differ in composition from those generated be energy production, and are created from processing Pu and tritium for nuclear weapons.[9] The acidic wastes are neutralized with NaOH and are temporarily stored in stainless steel tanks as liquid sludge. As a result, these wastes are highly concentrated with sodium and other metals such as Fe, Al, and Zr.

I.2. Nuclear Waste Forms

The storage of HLW involves a multiple barrier system. Firstly, the radioactive waste is immobilized in a waste form: a solidified body that captures the radionuclides within its structure. The waste form is placed inside a stainless steel canister for final storage in a deep underground repository. A summary of different materials for potential waste forms and the important properties of chemical durability and radiation damage are summarized in this section.

I.2.1 Glass-Based Waste Forms

Vitrification of HLW to form glasses was first popularized due to decades of experience and advancements in the glass melting industry. The advantages of using glass systems include: reasonably low processing temperatures (~1100 - 1300 °C), ability to tolerate fluctuations in waste stream composition, reasonable chemical durability, and high radiation stability that accommodates volume changes during radioactive decay.[10] The composition of glass-based waste forms is a compromise of waste solubility, formation temperature, and low leachability in water. However, low solubility of some actinides (Th, U, Pu, and Ce/Hf/Nd – actinide surrogates) in glasses resulting in high waste form volumes[11-13] has led to the exploration of alternative fabrication methods of waste forms.

Production of glass waste form is typically achieved through the use of joule melters,[14,15] which can produce several hundred kg/day. Although this is a large overall volume, actinides and Mo,[16-18] have low solubility as mentioned above, and decrease the waste loading, and reduce melter lifetime. The volatility of radioactive elements at these high temperatures must also be taken into account with off-gas systems and spent/failed melters also create large amounts of secondary radioactive waste that must be dealt with.

I.2.1.1 Borosilicate Glasses

As the basis of the commercial glass industry, silicate glasses are well characterized and understood. The compositions for waste forms are rich in B_2O_3 in order to substantially lower the processing temperatures required for glass formation. The flexibility of the compositions, allowing for tailoring of waste loading, glass forming ability, chemical durability, and radiation stability, has qualified borosilicate glasses to be the baseline and reference waste form for HLW. Select glass compositions in use in different countries are listed in Table I-2.[19]

Table I-2. Typical Borosilicate Glass Compositions Developed by Different Countries for HLW Immobilization

Oxide (wt%)	R7T7 (France)	DWPF (US)	Pamela (UK)	Belgium
SiO_2	54.9	68.0	58.6	68.5
B_2O_3	16.9	10.0	14.7	15.0
Li_2O	2.4	7.0	4.7	5.4
Na_2O	11.9	13.0	6.5	11.2
CaO	4.9	-	5.1	-
TiO_2	-	-	5.1	-
MgO	-	1.0	2.3	-
Al_2O_3	5.9	-	3.0	-
ZnO	3.0	-	-	-
ZrO_2	-	1.0	-	-

I.2.1.2 Other Glass-Based Waste Forms

Due to their low formation temperatures and solubility of sulphates (which cause phase separation in borosilicate glasses[20,21]) and lower formation temperatures,[22] phosphate glasses have been evaluated for this application. Both iron and lead phosphates[23-26] have been the topic of research for HLW immobilization. Despite these advantages, the low chemical durability and thermal stability make them poor choices for waste form applications.

I.2.2 Crystalline Waste Forms

To address the potential hazards associated with the thermodynamic instability and the large waste form volume due to low solubility of actinide elements, research into alternative waste form materials was initiated. Immobilization of HLW in crystalline ceramics stemmed from the presence of radionuclides found inside natural mineral structures. The range of elements found in HLW has led to the interest in many different crystalline phases such as barium hollandite,[27-29] perovskite,[30-32] zirconolite,[33-35]

pyrochlore,[36-38] and phosphates,[39-41] as well as multiphase assemblages of these phases, most importantly synthetic rock or SYNROC.[42-44] Immobilization of HLW in crystalline materials is achieved by direct substitution on a crystallographic site in the material structure, requiring detailed knowledge of solubility limits and crystal chemistry.

I.2.2.1 SYNROC

As proposed by Ringwood *et al.* in 1979, SYNROC, is comprised of titanate materials of hollandite, perovskite, and zirconolite phases as part of a multiphase assemblage.[42] The multiphase nature allows for fluctuations in the waste stream to be accommodated. A number of different compositions of SYNROC have been reported tailored for different waste streams; for example, SYNROC-C for waste generated from the reprocessing of spent nuclear fuel,[43] SYNROC-D for defense wastes,[44] and SYNROC-F for unprocessed spent nuclear fuel.[45] SYNROC materials are typically formed by hot-pressing under subsolidus conditions (1200-1400°C).[42]

For typical SYNROC-C compositions consisting of 40% hollandite, 35% zirconolite, and 25% perovskite, about 20 wt% HLW 'calcine' (liquid HLW calcined to remove excess acid from reprocessing) can be immobilized in the crystal structures.[43] The chemical durability of SYNROC is very high, suffering little corrosion after 532 days at 150°C submersed in deionized water.[46] SYNROC is predicted to be extremely radiation damage resistant, surviving 10^6 years before becoming amorphous, based on natural mineral analogues.[47]

I.2.3 Single Phase Waste Forms

Single phase ceramic waste forms have also been proposed to target select waste elements by portioning the reprocessed wastes or to immobilize the entire range of elements in the waste stream.

I.2.4 Zirconolite

As its name implies, zirconolite is targeted in the multiphase ceramic as the primary host for Zr. Zirconolite has a monoclinic structure and belongs to the C2/c space group. There are five cation (Ca, Ti and Zr) sites, three of which are occupied by Ti. Two of the

Ti sites are six-coordinated, and the third site is five-coordinated and has 50% occupancy.[33] The zirconolite structure is made up of alternating layers of Ti polyhedra and planes of Ca and Zr that lie parallel to (001) planes. The Ca and Zr atoms are aligned in alternating [110]-type rows with 8-fold and 7-fold polyhedra respectively. There is a rotation of 180° around the c axis between a pair of layers.[48] A detailed description of the zirconolite polymorphs can be found in Section V.

Actinide and rare earth elements (REEs) can substitutionally enter the structure on Ca and Zr sites.[49-53] Zirconolite materials are the major focus of the present thesis, thus summaries of elemental substitution and waste form performance properties are included in later sections of this thesis.

I.2.5 Pyrochlore

Pyrochlore is one of the ceramic phases of interest for the immobilization of nuclear waste due to its ability to incorporate actinides and REEs into its structure.[38,54,55] Pyrochlore has the composition of $A_2B_2X_6X'$, where A is a 2 or 3 + cation, B is a 4 or 5 + cation, and X and X' are anions (O^{2-}) [56]. The structure of pyrochlore is related to a fluorite $2 \times 2 \times 2$ superstructure and can be envisioned as built up layers of perovskite sheets.[57] The A ions are coordinated to eight oxygen atoms, the B ions are coordinated to 6 oxygen atoms, and one-eighth of the oxygen anion sites are vacant to maintain charge balance (8a site).[58] The pyrochlore structure is stable in the cubic form ($Fd\bar{3}m$) with a radius ratio (r_A/r_B) from 1.46 – 1.78, and the monoclinic structure forms when the ratio is greater than 1.78[59], as is the case with $Nd_2Ti_2O_7$ used in this thesis ($r_A/r_B = 1.83$).

Both Ti and Zr are typical elements used as 'B' cations, called titanate and zirconate pyrochlores. Titanate materials typically require lower processing temperatures, while zirconate materials possess superior radiation stability.[60-62] When zirconate pyrochlores are irradiated, an order-disorder transformation occurs forming a defect fluorite structure, and the irradiation resistance is increased.[63] The focus of this thesis is titanate pyrochlores to improve processing with spark plasma sintering (SPS).

I.2.6 Hollandite

Hollandite materials are used to immobilize fission products, such as Cs. In nuclear waste form application, the general formula is $[Ba_xCs_y][M^{3+}_{2x+y}Ti_{8-2x-y}]O_{16}$, where *M* is a trivalent cation.[64] Trivalent cations of interest include Al, Fe, Ga, Cr, and Sc,[65] although Cr additions promote Cs hollandite formation and aid in maintaining phase stability during processing.[66] The choice of trivalent cation also determines whether the unit cell symmetry is tetragonal (I4/m) or monoclinic (I2/m).[67] Hollandites exhibit a tunnel structure made up edge sharing and corner sharing $(M,Ti)O_6$ octahedra that accommodate the larger elements (Ba, Cs).[28,68] This structure allows for the accommodation of β-decay of ^{137}Cs ($^{137}Cs \rightarrow {}^{137}Ba + \beta(e^-)$ and $Ti^{4+} + \beta(e^-) \rightarrow Ti^{3+}$).[65] Cs is a long-lived fission product (^{135}Cs half-life of $\sim 2 \times 10^6$ years)[69] and heavily contributes to the build-up of heat in the waste form as radioactive decay occurs.

I.3. Composite Waste Forms

The idea behind glass-ceramics as waste forms is to combine the advantages of glasses and ceramics to create a superior waste form. They allow for flexibility in the waste stream composition compared to ceramics and potentially greater waste loading than glasses. The glass fraction of the material can also act as another barrier for radionuclides incorporated into the ceramic fraction.[70] Glass-ceramics for waste form applications are typically formed by pouring a glass melt, followed by controlled crystallization, which can be achieved through heat treatments or slow cooling of the melt.[71]

Zirconolite is a popular choice for the ceramic portion of the glass-ceramic.[72-74] Zirconolite can incorporate many of the elements (namely actinides) that have poor solubility in glasses, has good radiation damage resistance, and superior chemical durability. Additionally, it is not known for SiO_2 to enter into the zirconolite structure due to the absence of tetrahedral sites.[75]

Glass-ceramics demonstrate good chemical durability under leaching conditions. Ce containing iron-phosphate glass-ceramics have been fabricated by melting precursor oxides and cooling at a rate of 1.5°C/min from 1200°C. These glass-ceramics were subjected to the Product Consistency Test (PCT) and the obtained leach rates of Fe and Ce were 3.5×10^{-5} and 5.0×10^{-5} g/m^{2}day respectively after 56 days at 90°C.[76] Zirconolite-

containing glass-ceramics also exhibit high chemical durability with a leach rate of Nd of ~10^{-5} g/m^2day from materials prepared by post-melting annealing.[77]

Radiation damage, simulated by ion implantation, has been studied in select glass-ceramic compositions. Paknahad and Grosvenor[78] have reported a composite consisting of 30/70 wt% ceramic (brannerite and zirconolite)/borosilicate glass that is largely unaffected by implantation of Au ions to a dose of 5×10^{14} ions/cm. Another radiation stability test showed that under light ion irradiation, little change could be seen using X-ray diffraction (XRD) but under heavy ion irradiation amorphization of the crystallization phases occurs, as seen by XRD and transmission electron microscopy – selected area electron diffraction (TEM-SAED).[79]

I.4. Geological Disposal

The long-term storage of nuclear waste is proposed as deep geological disposal as part of a multi-barrier system.[80-82] The goal is to protect the biosphere from the toxicity of stored radioactive material and the location of the repository requires optimization for yearly rainfall, lack of seismic activity, separation from population centers, and, most importantly, approval of politicians and the public. The thermal stability of the buffer material is the main requirement, and as such, it should be kept below 100°C.[82] A schematic of a geological disposal site is shown in Figure I-1. The disposal tunnel is located about 2-3 km underground and contains backfill consisting of crushed rock and bentonite. Stainless steel canisters containing the fabricated waste forms are placed in disposal pits located beneath the tunnel and the negative space inside the pits is filled with compacted bentonite blocks.[82] These canisters also act as containment during transport to the repository.

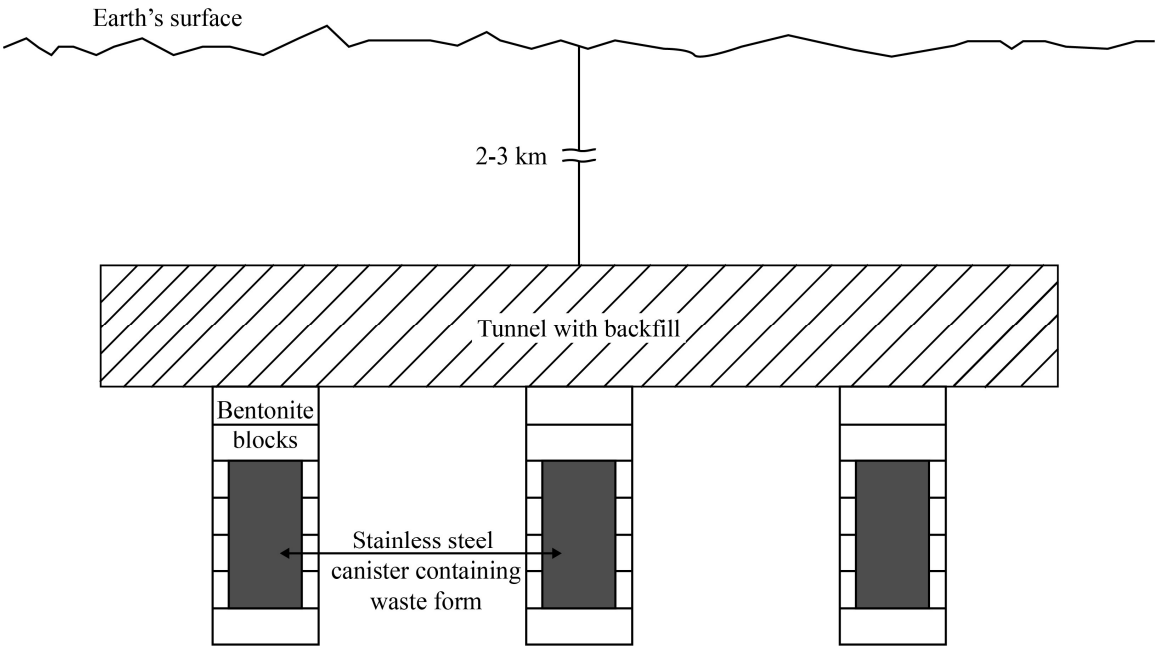

Figure I-1. Schematic of a geologic disposal site for nuclear waste.

An alternative disposal route is to place the waste canisters into a deep borehole. The concept is similar to that of disposal in a geological repository. A reference design details placing 400 canisters containing HLW forms in the lower 2 km of a borehole with a total depth of 5 km and the upper 3 km plugged with bentonite blocks and concrete.[83] Similar requirements for the location of this type of repository are needed as mentioned above, and are discussed in depth in a recent document released by Sandia National Laboratoy.[84] The technology exists to drill boreholes to this depth with large diameters (up to 100 cm).[85] The ability to retrieve and monitor waste is severely inhibited using deep boreholes as a disposal location.

I.5. Spark Plasma Sintering

SPS is of interest as an alternative densification technique because of the comparatively short processing time (on the order of minutes) that is required to achieve a dense ceramic. The short processing times (along with self-contained sample inside the die) can reduce the volatilization of waste elements. Uniaxial pressure and a DC current are simultaneously applied to a graphite die containing the powder sample. The current generates resistive heating of the graphite die (and the sample if electrically conductive),

which creates fast heating rates of up to 1000°C/min.[86] As shown in Figure I-2, the current flows through the graphite punches, across and into the cylindrical die, and back to the punch located below the sample. This is the typical current flow during SPS experiments, assuming the resistance of the sample is much greater than that of the graphite hardware. The SPS processing environment is inherently reducing, as it utilizes a graphite die. The process is capable of producing high-density samples compared to melt processing. SPS is limited by the small throughput that can be obtained with current equipment configurations and carbon diffusion from the die into the sample occurs at elevated temperatures.[86]

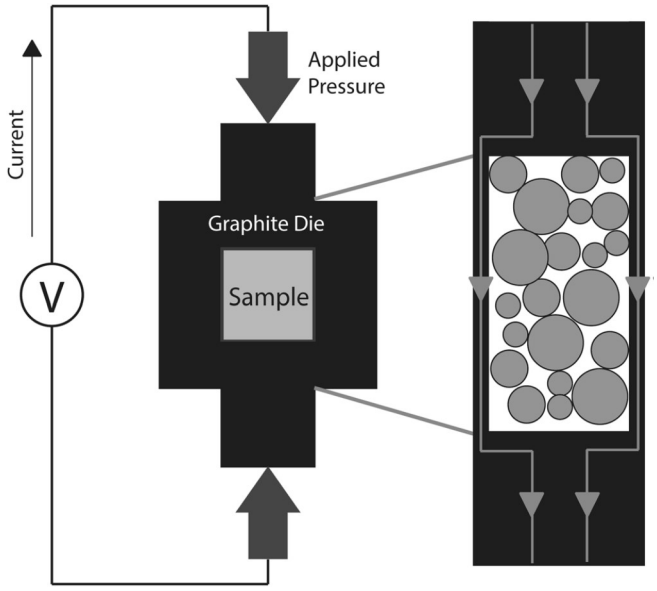

Figure I-2. Schematic of the graphite die setup in SPS.

I.6. Scope of this Study

This thesis focuses on the consolidation and characterization of multiphase and single phase waste form materials using SPS. This effort lays the groundwork for the scientific and technical studies of ceramic waste form materials using this processing method. This thesis is separated into two main parts, the first focusing on multiphase waste form assemblages and, the second, on single phases of zirconolite and pyrochlore.

Processing and characterization of multiphase ceramic waste forms focusing on the differences between materials formed by melt-processing and SPS is presented in the first part of this thesis (Sections III-IV). The phase assemblages and microstructures of the

simulated waste forms were characterized highlighting the similarities in phases present using the two processing techniques, while contrasting the microstructures that were formed. The radiation damage effects on these ceramic waste forms were simulated using ion beams, to determine possible processing advantages on this crucial waste form property.

The second part of this thesis (Sections V-VII) focuses on the incorporation of cerium (Ce) into single phases of zirconolite ($CaZrTi_2O_7$) and pyrochlore ($Nd_2Ti_2O_7$) to simulate the immobilization of rare earth elements and actinides. The zirconolite phase transition with increasing Ce loading, sintering behavior via SPS, and the waste form performance as defined by leach behavior/resistance and radiation damage are described in this part of the thesis.

II. MATERIALS AND METHODS

II.1. Compositions

II.1.1 Multiphase Compositions

Savannah River National Laboratory (SRNL) developed the multiphase waste form composition[87,88] and provided appropriate batch materials for our experiments. The multiphase composition was based on simulated waste stream compositions that are currently being investigated under the DOE Fuel Cycle Research and Development (FCR&D) program. Stoichiometric amounts of reagent-grade oxides and carbonates were blended together, mixed in de-ionized water with zirconia media, and dried at 90˚C. The resulting material was used as feedstock for our experiments. The target compositions, hereafter indicated as CAF- MP (Cr-Al-Fe-Multiphase) and Cr-MP (Cr-Multiphase), are listed in Table II-1.

Table II-1. Simulated Waste Form Compositions

Oxide	CAF-MP (wt%)	Cr-MP (wt%)
Al_2O_3	1.27	0.00
BaO	12.76	12.72
CaO	1.39	1.38
Cr_2O_3	6.33	14.5
CdO	0.11	0.11
Ce_2O_3	3.10	3.09
Cs_2O	2.88	2.87
Eu_2O_3	0.17	0.17
Fe_2O_3	6.65	0.00
Gd_2O_3	0.16	0.16
La_2O_3	1.58	1.58
MoO_3	0.85	0.84
Nd_2O_3	5.23	5.22
Pr_2O_3	1.45	1.44
Rb_2O	0.42	0.42
SeO_2	0.08	0.08
Sm_2O_3	1.08	1.07
SnO_2	0.07	0.07
SrO	0.98	0.98
TeO_2	0.66	0.65
TiO_2	49.16	49.01
Y_2O_3	0.63	0.63
ZrO_2	2.99	2.98

II.1.2 Cerium Substituted Zirconolite and Pyrochlore

Two major phases that appear in SYNROC materials are zirconolite and pyrochlore. To investigate waste loading and sintering of these materials for waste form applications, the compositions of $Nd_{2-x}Ce_xTi_2O_7$, x = 0-0.5 and $CaZr_{1-x}Ce_xTi_2O_7$, x = 0-0.5 were selected for our study. These compositional ranges encompass the solubility limit of Ce in zirconolite materials and is unexplored in neodymium titanate pyrochlores.

II.2. Multiphase Ceramic Sample Preparation

II.2.1 Melt-Processing

Melt-processing of multiphase ceramic waste forms was performed in an electrically heated tube furnace. Approximately 10g of the batched oxides, loosely packed in a Pt foil, were heated to 1500˚C at a rate of 5 °C/min, held for 30 minutes, and furnace-cooled back to room temperature. The solidified material was removed from the foil and used for characterization.

II.2.2 Spark-Plasma Sintering (SPS)

For multiphase ceramic waste forms, reactive SPS was carried out using a FCT HP D 25 (FCT Systeme GmbH, Rauenstein, Germany) furnace with graphite dies and punches (I-85 grade, Electrodes Inc., CT, USA). Figure I-2 presents the schematic of the die setup. Unreacted batched powder (~3g) was enclosed within a thin graphite foil and placed inside a graphite die. The reactive sintering was performed under a pressure of 54 MPa by heating to a maximum temperature of 1000˚C (CAF-MP) or 1040°C (Cr-MP), as read by an optical pyrometer focused on the outside of the die, at a heating rate of 100 °C/min, holding for 3 minutes, and cooling at a rate of 100 °C/min.

II.3. Single-Phase Sample Preparation

II.3.1 Solid-State Sintering

Single-phase zirconolite and pyrochlore materials were synthesized using conventional solid-state techniques. Stoichiometric amounts of commercially available high purity oxides were weighed and mixed using ball-milling according to the compositions found in Section II.1.2. The milling procedures for the zirconolite and

pyrochlore materials were different due to the slow reaction rate of the zirconolite compared to pyrochlore.

For zirconolite materials, the weighed oxides were placed in a ZrO_2 milling jar with 2 mm YSZ milling media (Across International, NJ, USA). The precursors were milled at 1,200 rpm using a mixture of ethanol and water as the milling medium in a VQ-N High Speed Ball Mill (Across International, NJ USA) for 15 min. The resulting slurry was separated from the media and dried on a hot plate. The dry powders were homogenized using a mortar and pestle and pressed into 20 mm diameter pellets using a hydraulic press and a steel die. The pellets were allowed to react in a furnace at 1375°C for 72 h, crushed into powder, milled for 5 min using the same procedure, dried, and homogenized with a mortar and pestle.

For pyrochlore materials, the weighed out oxides were placed in a high-density polyethylene (HDPE) jar with 1/4 inch spherical alumina media and ethanol/water mixture. Milling was performed for one hour. The media was removed from the slurry and the slurry was dried. The powders were homogenized and pressed into pellets as above. The pellets were allowed to react in a furnace at 1400°C for 24 h, crushed, pelletized and reacted a second time at 1400°C for 24 h. The resulting pellets were crushed and homogenized for characterization.

II.3.2 Spark-Plasma Sintering (SPS) of Pyrochlore and Zirconolite

SPS of pyrochlore and zirconolite materials was carried out using the same instrument and die setup as described in Section II.2.2. Pyrochlore materials ($Nd_{2-x}Ce_xTi_2O_7$, x = 0-0.5) were sintered by heating at 100°C/min to a maximum temperature of 1225°C, holding at temperature for 30 s, cooling at 100°C/min, and applying 54 MPa pressure throughout the cycle. High density (>98% theoretical density) pellets are obtained using this sintering schedule.

Zirconolite materials ($CaZr_{1-x}Ce_xTi_2O_7$, x = 0-0.5) were sintered by heating at 100°C/min to a maximum temperature of 1100°C, holding at temperature for 300 s, cooling at 100°C/min, and applying 98 MPa pressure throughout the cycle. Phase transformation occurs during the SPS process, making density calculations difficult. The SPS schedules of both materials are displayed graphically in Figure II-1.

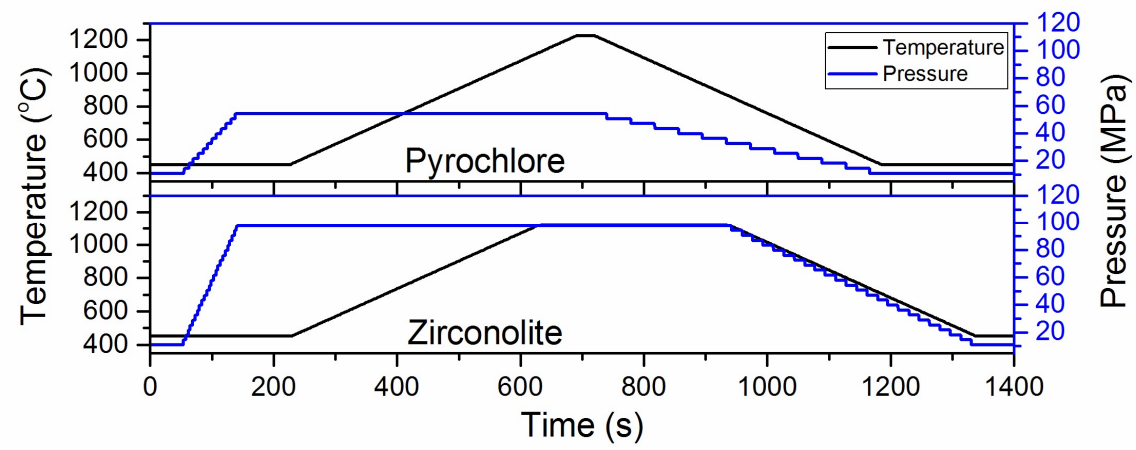

Figure II-1. SPS schedules used for pyrochlore and zirconolite materials.

III. PHASE ASSEMBLAGE AND MICROSTRUCTURE OF MULTIPHASE CERAMIC WASTE FORMS

Hollandite-rich ceramic waste forms have been demonstrated to exhibit high durability while simultaneously accommodating a wide range of radionuclides in their matrices. This section presents results on the preparation and characterization of ceramic waste forms prepared by two different methods – melt processing and SPS. Both processes resulted in similar phase assemblages but exhibited different microstructures depending on processing method. The SPS samples exhibited fine grained (< 1 μm) and dispersed phases, whereas the melt processed sample contained larger grains (10-20 μm) of specific phases. Microstructural analysis was performed using SEM, EDS, and WDS.

III.1. Introduction

There are many proposed waste form technologies for the storage of nuclear waste, including thermal and non-thermal processes. These consist of, but are not limited to, vitrification,[89] hot isostatic pressing,[90] melt formation,[66] spark plasma sintering,[90] and cementation.[91] Titanate-based ceramic waste forms specifically SYNROC[42,92,93] and derivative materials have been widely studied for their potential to accommodate a large variety of radionuclides.

III.2. Methodology

III.2.1 Characterization

Powder XRD data was collected for phase identification using a D-2 Phaser (Bruker, Massachusetts, USA). The microstructure of polished sections was observed using a FEI™ Quanta 200 F scanning electron microscope (FEI, Hillsboro, Oregon, USA). Further phase assemblage and elemental distribution were studied by wavelength dispersive spectroscopy (WDS). Selected elemental maps from multiphase regions, identified from back-scattered electron (BSE) images, were collected using JEOL JXA-8200, WD/ED Combined Electron Probe Microanalyzer (EPMA) (JEOL Ltd., Tokyo, Japan). Elemental scans were performed at an accelerating potential of 15kV, with a step size of 0.5μm in *x*- and *y*- directions, and a dwell time of 80 milliseconds at each point.

III.3. Results and Discussion

III.3.1 Phase Assemblage

Figure III-1 shows the XRD patterns of the two compositions fabricated by SPS and melt-processing. Similar phase assemblage is seen in all samples, with hollandite as the major phase, along with perovskite and a zirconium-rich phase. The melt-processed samples contain some TiO_2, while the CAF-MP sample processed by SPS contains some CeO_2.

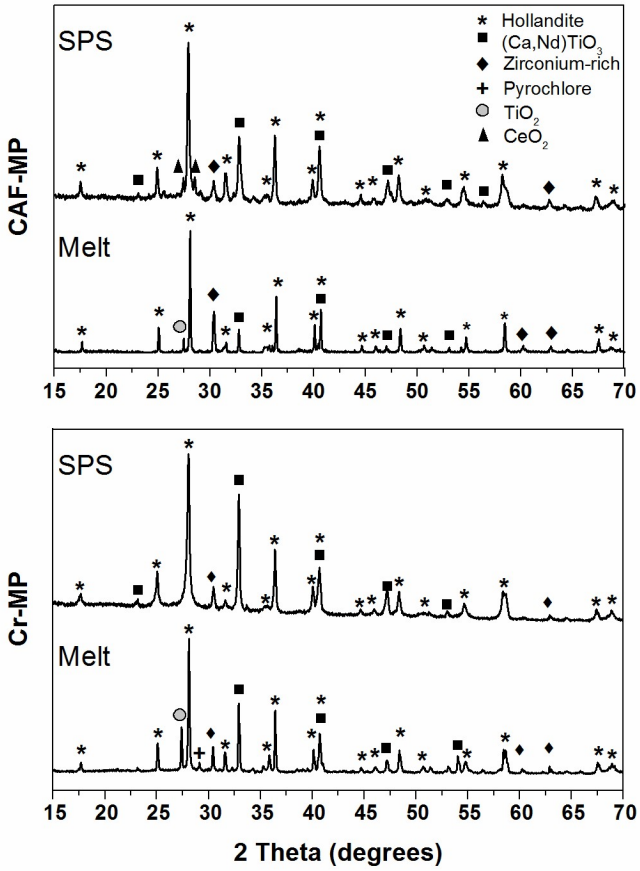

Figure III-1. XRD patterns of CAF- and Cr-MP samples produced by SPS and melt-processing.

Contrary to the phase formation results, the microstructures of the samples using the two processes were dissimilar. Figure III-2 compares the two microstructures with BSE images. The sample processed by SPS shows a fine grain structure with highly dispersed phases amongst the matrix (hollandite). In contrast, the melt-processed sample contains

larger islands of the different phases that are aggregated to each other. Similar microstructures are seen in the Cr-MP samples.

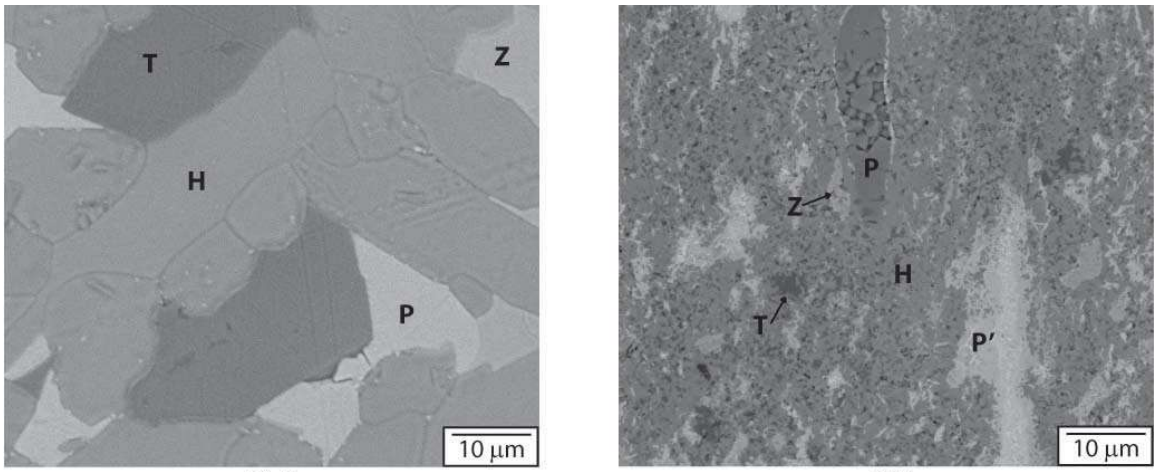

Figure III-2. Microstructures of SPS and melt-processed CAF-MPB samples with phase fields indicated. H = hollandite, P and P′ = perovskite, Z = zirconium-rich, and T = TiO_2

III.3.2 Elemental Distribution

The phases seen in the microstructures were identified using a combination of WDS maps and XRD patterns. The appropriate phase fields are indicated in the images. Hollandite phase is represented with H, perovskite with P and P′, a zirconium-rich phase with Z, and TiO_2 with T. It should be noted that the identification of the zirconium-rich phase (Z) is inconclusive from a combination of EDS and XRD analysis. This phase may also belong to a zirconolite. Figure III-3 and Figure III-4 compare the WDS maps of selected elements in these multiphase samples.

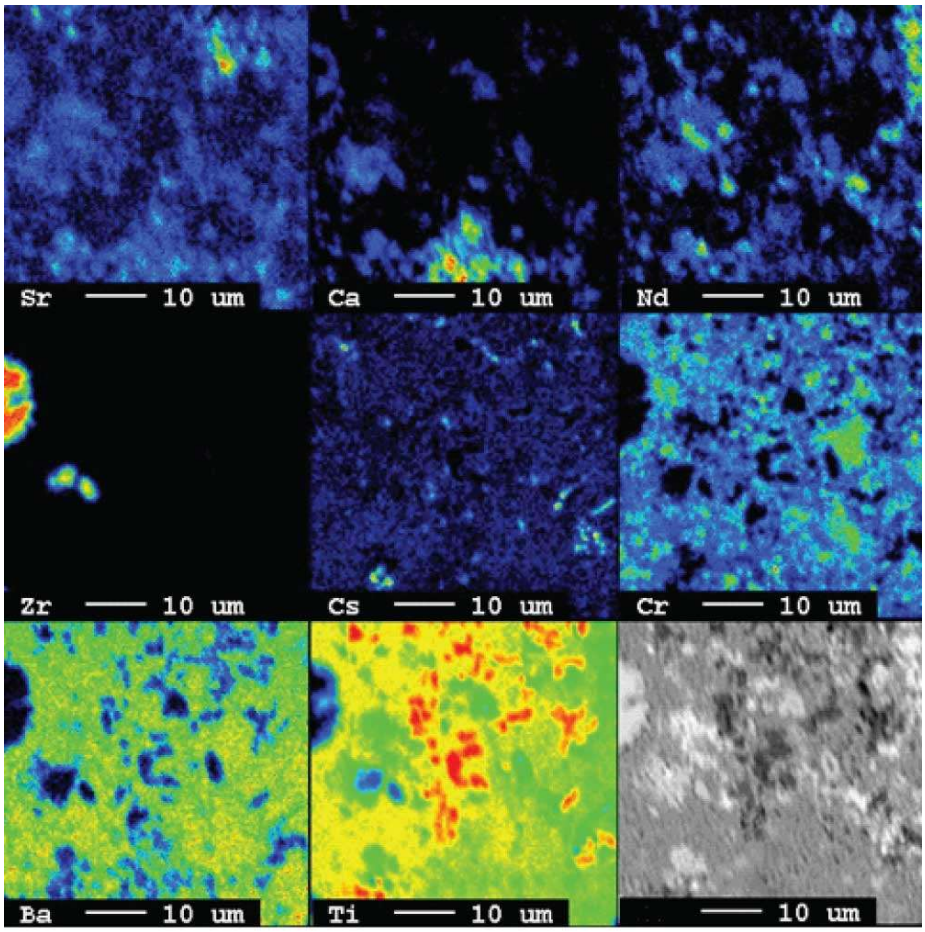

Figure III-3. Selected elemental maps by WDS in CAF-MP prepared by SPS.

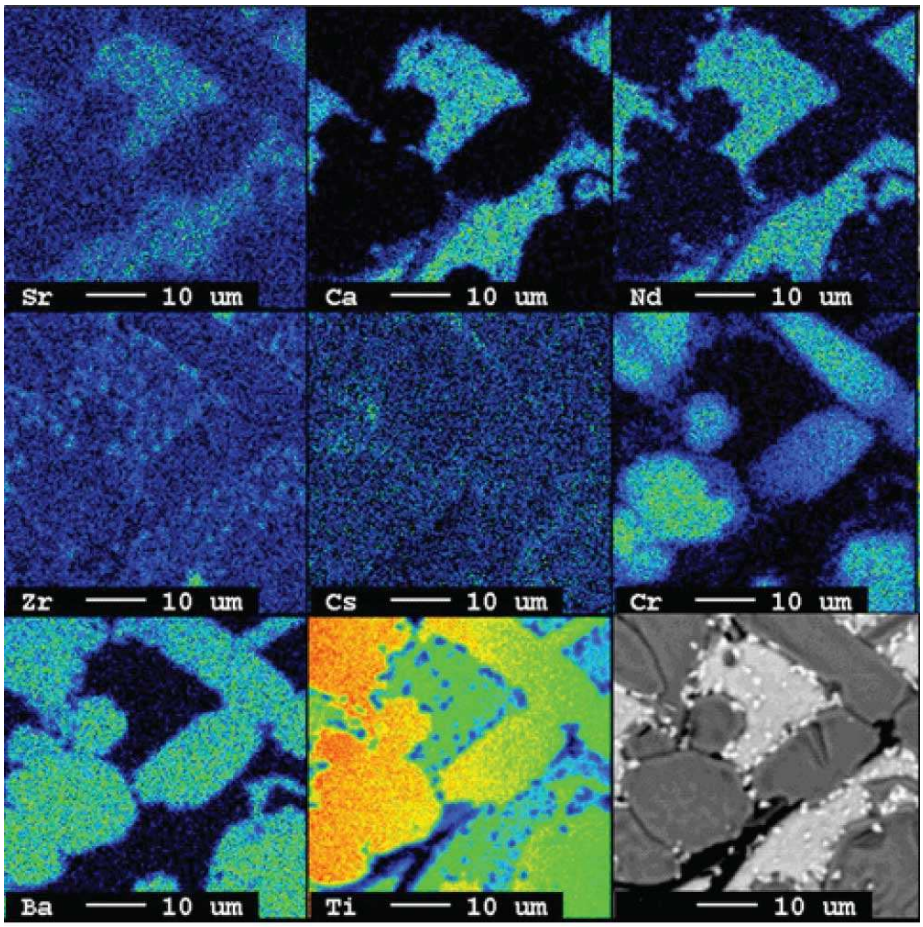

Figure III-4. Selected elemental maps by WDS in CAF-MP prepared by melt processing.

In the SPS sample, hollandite formed the matrix of the sample and the remaining phases were dispersed throughout. The inter-dispersed phases ranged in size from < 1 μm to ~10 μm. WDS measurements revealed two separate perovskite phases present, a gray colored phase and a brighter phase, denoted P and P′ respectively in the Figure III-2. The gray phase was rich in Fe, while the bright phase was rich in REEs such as Nd, in agreement with expected atomic mass ratios. A small amount of a cerium and titanium rich phase was seen in EDS, corresponding to the CeO_2 observed in the XRD pattern. The WDS results corroborate that hollandite makes up the matrix and that multiple perovskite phases are present, some high in alkaline earth elements (Sr and Ca) and other high in REE such as Nd. The zirconium-rich phase consists mainly of Zr and very little Sr (of the elements that were observed in WDS), indicating that this phase might be a solid solution of ZrO_2 and other oxides such as SrO. The WDS map of Cs did not show that the Cs is contained within

the hollandite grains, but rather that it is concentrated in certain areas, indicating the possibility of an undesirable Cs-rich phase.

Initial visual observation of the melt-processed samples indicated that the samples were fully melted. Different phases were crystallized from the melt, with retention of some unreacted TiO_2. Significant porosity was observed in the microstructure. Small amounts of Cs were detected in WDS mapping (Figure III-4) that appeared to be segregated towards the grain boundaries of hollandite phase. From all the WDS maps in Figure III-4, it could be observed that hollandite phase has elements predominantly Ba, Cr, Ti, O and Cs as per the target composition. All other elements like Ca, Sr, Nd, Ti partitioned together into the bright perovskite phase, suggesting that different perovskite and pyrochlore phases could be formed in the process hosting different elements, actinides, and rare-earth elements (REEs) in their lattices.

III.4. Conclusions

Compositions of simulated multiphase waste forms were processed by melt-processing and SPS, resulting in a hollandite-rich rich ceramic also containing perovskite and pyrochlore-zirconolite phases. XRD and WDS revealed small amounts of unreacted CeO_2 present in SPS processed samples. Cs partitioning into the hollandite phase was observed in melt-processed samples but was absent in SPS samples, leading to the formation of Cs-rich phases. Multiple perovskite phases were seen in SPS processed waste forms, one high in alkaline earths, and one rich in rare earth elements. This study shows that multiphase waste forms can be produced through melt-processing and SPS with desired phase assemblages, although the SPS process requires optimization to eliminate Cs-rich phases.

IV. RADIATION DAMAGE OF HOLLANDITE IN MULTIPHASE CERAMIC WASTE FORMS

Radiation damage was simulated in multiphase titanate-based ceramic waste forms using an ion accelerator to generate high energy alpha particles (He^{+}) and an ion implanter to generate 7 MeV gold (Au^{3+}) particles. X-ray diffraction and transmission electron microscopy were used to characterize the damaged surfaces and nearby regions. Simulated multiphase ceramic waste forms were prepared using two processing methods: SPS and melt-processing. Both processing methods produced ceramics with similar phase assemblages consisting of hollandite-, zirconolite/pyrochlore-, and perovskite- type phases. The measured heavy ion (Au^{3+}) penetration depth was less in spark plasma sintered samples than in melt-processed samples. Structural breakdown of the hollandite phase occurred under He^{+} irradiation and the composition of the constituent hollandite phase affected the extent of damage induced by Au^{3+} ions. These results are summarized in this section.

IV.1. Introduction

Ceramics have been shown to be susceptible to damage induced by α-radiation.[31,94,95] Specifically, α-radiation can induce atomic displacements that lead to structural rearrangements affecting the physical and chemical properties of the material. An α-decay event consists of the release of an α-particle (light particle) and a recoil nucleus (heavy particle). Actinides and their daughter products have long half-lives and therefore α-decay becomes dominant over long time scales. This necessitates the use of ion implantation techniques to study the effects of α-decay on a laboratory time scale.

The α-particles and recoil nuclei interact with materials in different ways. The α-particles transfer their energy primarily through electronic stopping (ionization) and deposit their remaining energy through ballistic processes at the end of their track. In contrast, recoil nuclei transfer their energy primarily through nuclear stopping depositing their energy a considerably shorter distance or volume than α-particles. Normally, recoil nuclei produce several thousand displacements in a localized area (dense cascade), while α-particles generate several hundred displacements over a greater travel (dilute cascade).[96]

One method to study these differing damage mechanisms uses He^+ ions to simulate α-particles and heavy ions, such as Au^{3+} or Kr^{3+}, to simulate α-recoils.

Charged particle implantation has been widely utilized to study radiation damage in crystalline ceramics.[97-101] However, relatively few studies have been performed on multiphase crystalline ceramics for nuclear waste immobilization of a combined waste to include a Cs/Sr separated waste stream, the Trivalent Actinide - Lanthanide Separation by Phosphorous reagent Extraction from Aqueous Komplexes (TALSPEAK) waste stream, the transition metal fission product waste stream resulting from the Transuranic Extraction (TRUEX) process, MoO_3, and noble metals.[47,79,102,103] Although the materials modeled were inert matrix fuel and not waste forms, Men *et al*. [104] studied the radiation response of a four-phase oxide ceramic composite using Au and Xe ions. The Al_2O_3, Y_2O_3 stabilized ZrO_2, and $MgAl_2O_4$ phases exhibited high amorphization resistance when irradiated with 10^{20} ions/m^2 10 MeV Au ions and 10^{16}-10^{17} ions/m^2 Xe ions, while $LaPO_4$ (monazite) melted and wet the other phases under Au irradiation but was unaffected by Xe irradiation.

IV.2. Methodology

IV.2.1 Ion Implantation Experiments

The experiments using Au^{3+} ions were carried out at room temperature at the Environmental Molecular Sciences Laboratory (EMSL), Pacific Northwest National Laboratory (PNNL) and the experiments using He^+ ions at the Ion Beam Materials Lab (IBML), Los Alamos National Laboratory (LANL) for the multiphase materials. 7 MeV Au^{3+} implantations were performed at EMSL on a National Electrostatics Corporation (NEC) model 9SDH-2 3.4 MV tandem accelerator[105] simulating three damage levels in SPS samples: 0.05, 0.5 and 5 dpa and one damage level, 5 dpa, in melt-processed samples. The unit dpa is used to compare radiation damage of materials. It represents the number of atoms displaced from their normal lattice sites as a result of energetic particle bombardment. These values were chosen to simulate varying storage times, from approximately 10^2-10^6 years.[106] The implanted area was 6 × 6 mm for both melt-processed and SPS samples. 200 keV He^+ implantations were performed at IBML using a 200 kV Danfysik high current ion implanter at a dose of 5 dpa to simulate α-particle damage after long storage times. 380 keV He^+ and 3 MeV Kr^{3+} implantations were performed on single

phase hollandite using the Ion Beam Laboratory (IBL) at the University at Albany. Single phase hollandites received doses of 0.5 dpa of either He^{+} or Kr^{3+} ions. The details of implantation experiments are summarized in Table IV-1.

Table IV-1. Summary of Ion Implantation Experiments

Composition	**Processing Method**	**Ion (Energy)**	**Fluence/dpa (ions/m^2)**
CAF-MP	Melt	Au (7 MeV)	1.4×10^{19}/5
CAF-MP	SPS	Au (7 MeV)	1.4×10^{19}/5
CAF-MP	SPS	Au (7 MeV)	1.4×10^{18}/0.5
CAF-MP	SPS	Au (7 MeV)	1.4×10^{17}/0.05
CAF-MP	SPS	He (200 keV)	2.0×10^{21}/5
Cr-MP	Melt	Au (7 MeV)	1.3×10^{19}/5
Cr-MP	SPS	Au (7 MeV)	1.3×10^{19}/5
Cr-MP	SPS	Au (7 MeV)	1.3×10^{18}/0.5
Cr-MP	SPS	Au (7 MeV)	1.3×10^{17}/0.05
Cr-MP	SPS	He (200 keV)	2.0×10^{21}/5
Cr-HOL	SSS	He (380 keV)	2.8×10^{20}/0.5
Cr-HOL	SSS	Kr (3 MeV)	2.0×10^{18}/0.5

IV.2.2 Sample Preparation and Damage Calculations

Samples for ion irradiation experiments were prepared by polishing a surface to 1 μm using a diamond suspension. The radiation dose in these materials was estimated using the Stopping and Range of Ions in Matter (SRIM) program.[107] The dpa as a function of depth for CAF-MP (similar results are obtained for Cr-MP) using 7 MeV Au^{3+} and 200 keV He^{+} is shown in Figure IV-1. The peak in dpa (5, 0.5 or 0.05) is located at 870 nm (Au^{3+}) and 700 nm (He^{+}). The dpa is adjusted by changing the fluence of the incoming gold ions (ions/cm^2). Single phase hollandites received doses of 0.5 dpa of either He^{+} or Kr^{3+} ions.

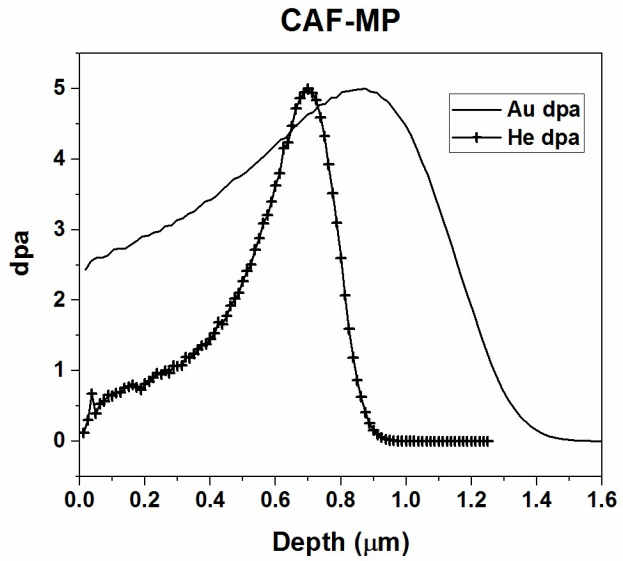

Figure IV-1. Damage profile in CAF-MP using 7 MeV Au^{3+} and 200 keV He^{+} ions.

IV.2.3 Single-Phase Hollandite Preparation

Single phase Cr-hollandite ($Ba_{1.15}Cr_{2.3}Ti_{5.7}O_{16}$, designated Cr-HOL) was produced via solid state sintering of stoichiometric amounts of commercially available oxides/carbonates that were mixed, ball-milled and dried at ~ 120˚C to form the precursor batch. The resulting powders were compacted into pellets and subsequently sintered at 1100˚C for 4h.

IV.2.4 Characterization

Grazing incidence x-ray diffraction (GIXRD) was performed on implanted samples using a grazing angle of 2° on the EMSL (Au^{3+}) samples and 1° for the LANL (He^{+}) samples with a Bruker AXS D8 Advance (Bruker, Massachusetts, USA) instrument using Cu Kα radiation in theta – 2 theta geometry. The unirradated areas of the Au^{3+} samples were visible and ground off prior to measurement. Damaged cross-section specimens were prepared for transmission electron microscopy (TEM) by using the lift-out method with a focused ion beam (FIB). The damaged areas were examined using a FEI Tecnai F20 TEM operating at 200 kV.

IV.3. Results and Discussion

IV.3.1 Heavy Ion Irradiations

Figure IV-2 shows the GIXRD patterns of CAF- and Cr- MP samples prepared using SPS and melt-processing subjected to 7 MeV Au^{3+} at a fluence corresponding to 5 dpa. All samples exhibited amorphization evidenced by a decrease in intensity of the diffraction peaks and the presence of diffuse scattering between 26 and 35 °2θ. CAF-MP samples produced by both processing routes show complete amorphization at 5 dpa, as demonstrated by the disappearance of all diffraction peaks. There is no new phase formation identified within the detectable limits (~5 wt%) of the technique. The highest intensity peaks of the major phases in Cr-MP samples are labeled in Figure IV-2. By comparing the intensity of these peaks, the TiO_2 and perovskite phases in the Cr-MP melt-processed are the least affected by the damage, indicating that the hollandite phase is more prone to heavy ion radiation damage. Previous results have shown that hollandite materials are susceptible to damage via heavy ion irradiation.[108]

Bright field TEM images of damaged cross-sections of both melt-processed and SPS CAF-MP samples irradiated with 7 MeV Au^{3+} to 5 dpa are shown in Figure IV-3. The corresponding selected area diffraction (SAD) patterns confirm that amorphization occurs in samples fabricated by both methods. Due to the large grain sizes in the melt-processed samples, only a hollandite grain was extracted with FIB, confirmed through indexing of the SAD pattern (space group C2/m, grain oriented in the [010] direction) and EDS (Figure IV-3). The amophized region in the hollandite grain was approximately 2.1 μm in depth. Cu present in the EDS spectra was attributed to the sample grid holder.

In contrast to the melt-processed samples, multiple grains are contained within the FIB sample of CAF-SPS. This was confirmed by examining the SAD pattern in the crystalline region (Figure IV-3). The pattern was unable to be indexed properly due to the interaction of the beam with multiple grains. The amorphized region of the SPS sample extended approximately 1.8 μm from the surface. The penetration depth of the Au^{3+} ions was greater in the melt-processed than that in the SPS fabricated sample. This was attributed to the interaction of the ions with multiple phases of much smaller (<1 μm) grain sizes. Grain boundaries act as sinks for radiation damage induced defects, therefore inhibiting ion penetration in SPS materials.[109] The ion penetration depth in both samples

was greater (~0.4 um) than that predicted by SRIM however, underestimation is not unprecedented such as of Au ion penetration investigated in SiC.[110]

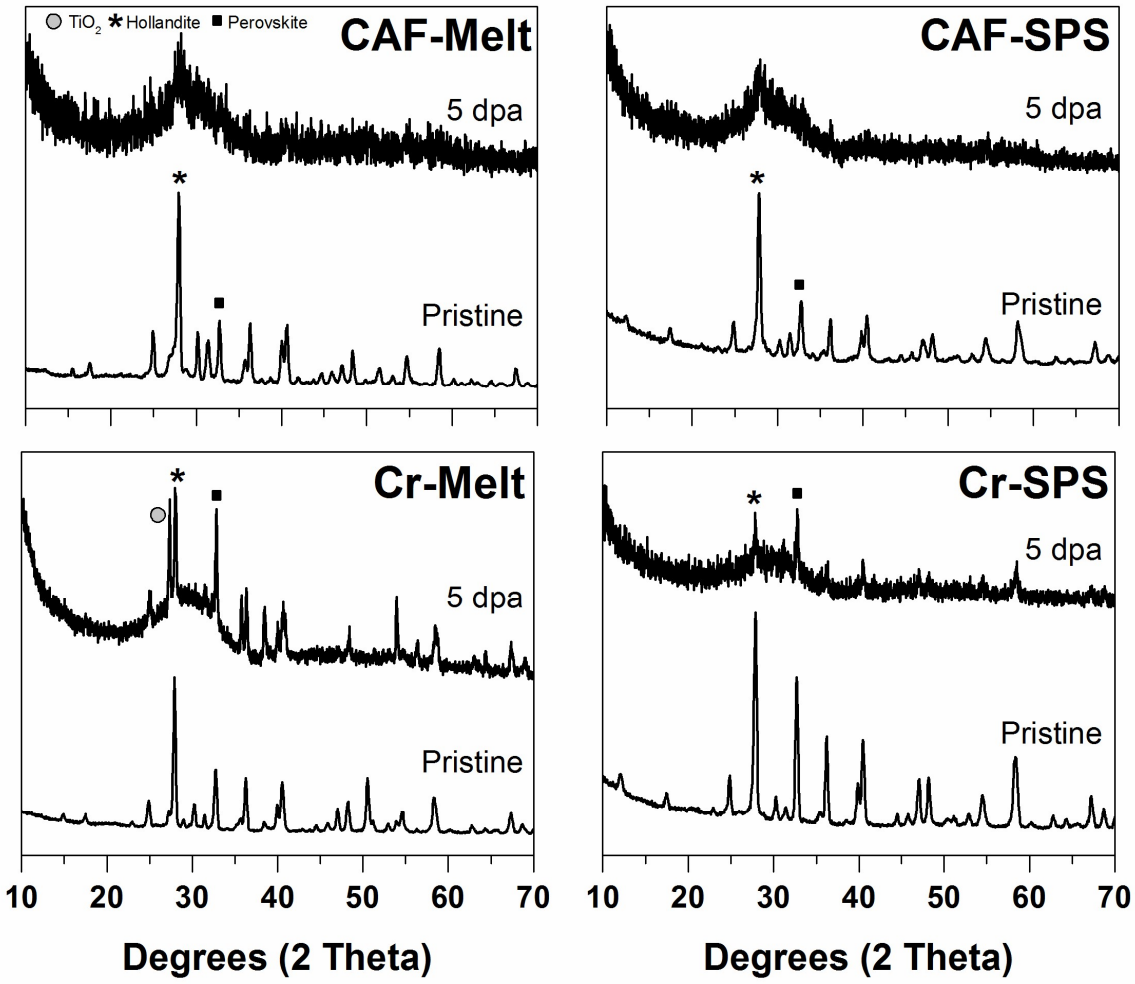

Figure IV-2. GIXRD of CAF- and Cr-MP samples fabricated by SPS and melt-processing exposed to 5 dpa of Au^{3+} ions.

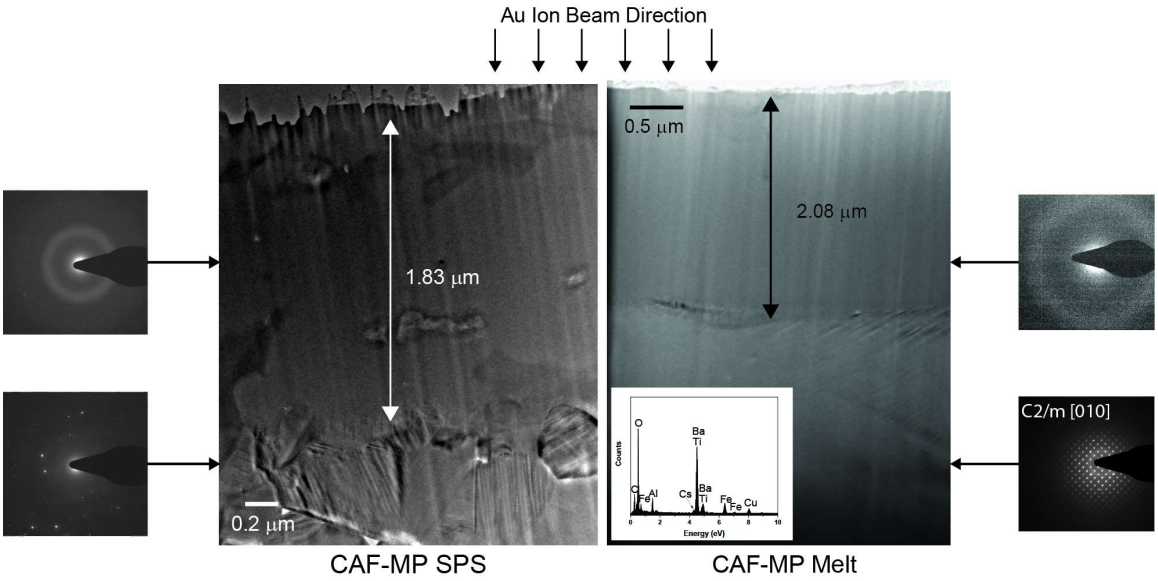

Figure IV-3. TEM images and corresponding SAD patterns of the damage cross-sections in CAF-MP materials prepared by melt-processing and SPS after exposure to 5 dpa of Au^{3+} ions.

GIXRD patterns for the samples fabricated by SPS and subjected to 3 different fluences of 7 MeV Au^{3+} ions corresponding to 0.05, 0.5, and 5 dpa are shown in Figure IV-4. Amorphization increased with increase in dpa as would be expected and only minor changes in the diffraction patterns were observed in samples exposed to a fluence corresponding to 0.05 dpa, suggesting a threshold fluence that lies above this level. At 0.5 dpa a marked decrease in peak intensity and diffuse scattering can be seen. Complete amorphization is observed in CAF-MP compositions at 5 dpa, while Cr-MP displayed an increase in diffuse scattering.

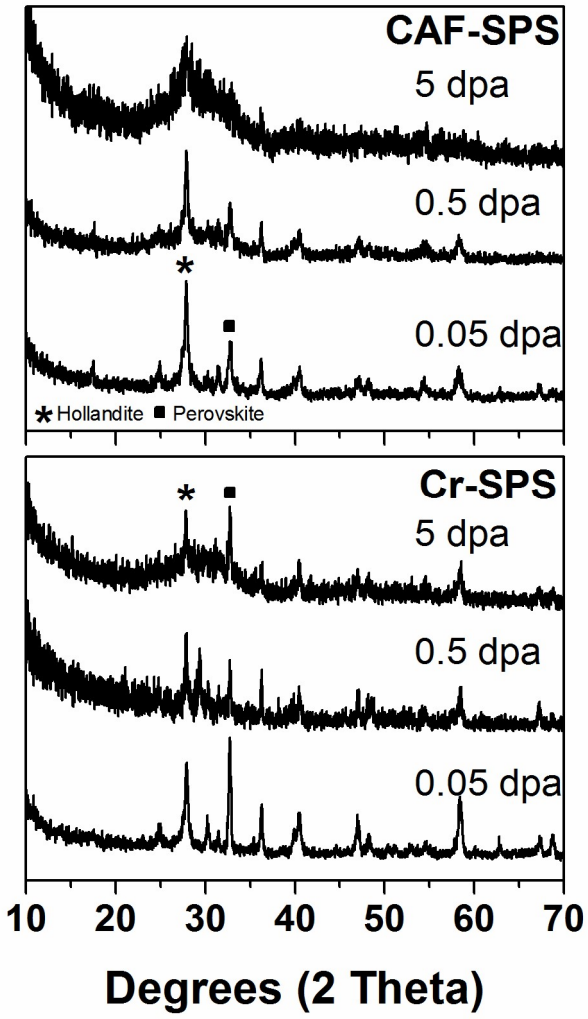

Figure IV-4. GIXRD of CAF- and Cr-SPS samples irradiated to 3 different damage levels with Au^{3+} ions.

IV.3.2 Light Ion Irradiations

GIXRD patterns for the SPS samples exposed to 200 keV He^{+} ions corresponding to 5 dpa are shown in Figure IV-5. In these patterns, diffuse scattering is seen from 26 and 35 °2θ indicating amorphization, and diffraction peaks not present in the pristine sample were identified and could be indexed to $Ba_2Ti_9O_{20}$. This $Ba_2Ti_9O_{20}$ phase is related to the hollandite phase in which some of the Ba ions are located on O sites, disrupting the tunnel structure of hollandite.[111,112] The presence of these new diffraction peaks, along with the disappearance of the diffraction peaks belonging to the hollandite phase, suggests that structural rearrangement of the hollandite phase occurs along with amorphization under

these irradiation conditions. The perovskite phase could be identified after irradiation and did not appear to amorphize as severely as the hollandite phase when irradiated with He^+ ions, indicating radiation stability under light ion irradiation up to 5 dpa. The zirconolite/pyrochlore (zirconium-rich) phase exhibited a relatively low-intensity diffraction pattern that could not readily be identified from the diffuse scattering.

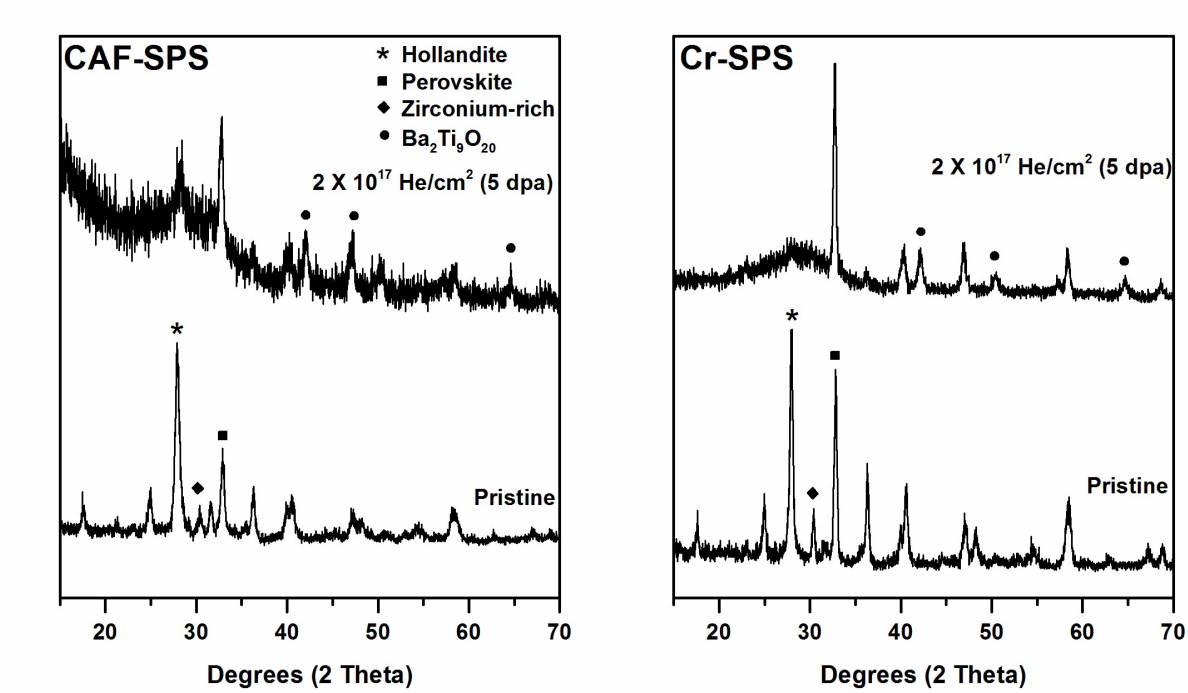

Figure IV-5. GIXRD of CAF- and Cr-MP SPS samples irradiated with 5 dpa He^+ ions.

IV.3.3 Comparison to Single Phase Hollandite

To further study the response of hollandite in the multiphase assemblages, single phase hollandite (Cr-HOL) was irradiated with Kr^{3+} (heavy) and He^+ (light) to doses equivalent to 0.5 dpa. GIXRD patterns from the pristine and irradiated surfaces of single phase hollandite are shown in Figure IV-6. The single-phase hollandite exhibited a behavior similar to that of hollandite within the multiphase assemblages. 0.5 dpa He and Kr both resulted in amorphization similar to multiphase samples as evidenced by diffuse scattering. He^+ irradiations also induced phase evolution as evidenced by the emergence of diffraction peaks corresponding to TiO_2, $BaTiO_5$, and $Ba_2Ti_9O_{20}$. The presence of the

TiO_2 and $BaTi_2O_5$ diffraction peaks suggests that the hollandite phase experiences structural breakdown when irradiated with light ions. The intensity of the $Ba_2Ti_9O_{20}$ diffraction peaks is reduced in Cr-HOL compared to that in the multiphase samples, indicating that the transition from hollandite structure to $Ba_2Ti_9O_{20}$ is incomplete at 0.5 dpa He^+ ions.

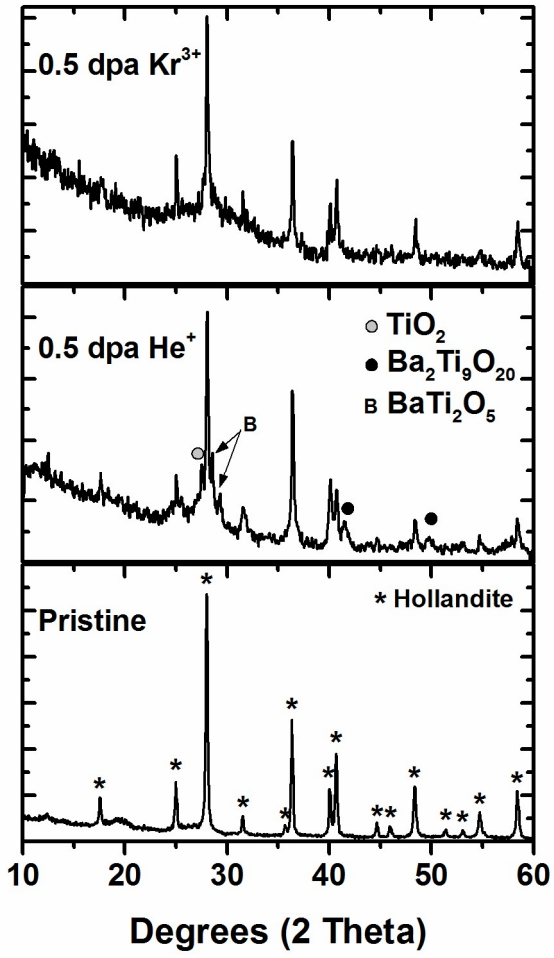

Figure IV-6. GIXRD patterns of single phase hollandite materials irradiated with 0.5 dpa Kr^{3+} and He^+ ions.

IV.4. Conclusions

Heavy and light ion implantation was used to induce damage in simulated multiphase ceramic waste form materials produced from SPS and a melt-process. The multiphase waste forms responded differently under the two different irradiation conditions. Under heavy ion (Au^{3+}) irradiation, the displacements initiated by the ballistic processes cause bulk material to amorphize. Under light ion (He^{+}) irradiation, the hollandite phase appeared to break down, while the other phases remained crystalline as evidenced by emergence of diffuse scattering and new crystalline phases at the expense of hollandite. Samples fabricated by both melt-processing and SPS exhibited similar amorphization behavior when irradiated with Au^{3+} ions although the penetration depth of Au^{3+} ions was less material fabricated by SPS compared to melt-processing. This is attributed to the smaller grain sizes of the phases in the SPS materials; the grain boundaries act as sinks for the radiation induced defects. The lower dose of He^{+} ions was demonstrated as a reliable way to render structural changes in the hollandite phase to be captured in the GIXRD patterns.

V. CERIUM SUBSTITUTION AND SPARK PLASMA SINTERING OF ZIRCONOLITE ($CaZrTi_2O_7$) AND PYROCHLORE ($Nd_2Ti_2O_7$)

Compounds with the formulae $CaZr_{1-x}Ce_xTi_2O_7$ and $Nd_{2-x}Ce_xTi_2O_7$ with x = 0.1-0.5 were synthesized by solid state reaction. Cerium was used as a surrogate for actinide elements. A transition from the 2M polymorph to the 4M polymorph (expanded unit cell due to cation ordering) in zirconolite was observed with increasing cerium content. The presence of both tri- and tetravalent Ce, contrary to formulation, was confirmed using X-ray absorption near edge spectroscopy (XANES), suggesting substitution on both Ca and Zr sites. Sintering was carried out via SPS, during which the perovskite phase ($Ca_{0.4}Ce_{0.4}TiO_3$) was stabilized due to the reducing conditions of this technique. SEM and EDS revealed that the 2M polymorph was dilute in Ce content in comparison to the 4M-zirconolite. High temperature XRD was used to detail the kinetics of perovskite to zirconolite transition. It was found that $CaCeTi_2O_7$ (cubic pyrochlore) forms as an intermediate phase during the transformation. Our results show that a transition from 2M- to 4M-zirconolite occurs with increasing Ce content and can be controlled by adjusting the P_{O2} and the heat treatment temperature.

V.1. Introduction

Cerium oxide is typically used as a surrogate for plutonium oxide (and other actinide elements) in simulated nuclear waste forms[113] due to the similar electronic structure, ionic size, and multiple valence states of both Ce and Pu. Both Ce and Pu can form tetravalent oxides with a fluorite structure and a trivalent phosphate with a monazite structure when heated in air between temperatures of 1000-1400°C,[114] demonstrating similar reduction potential of the two elements even in an oxidizing atmosphere; however, it should be noted that the propensity to reduce is higher for Ce. Cerium oxide has been deemed as a 'suitable' surrogate for plutonium oxide by researchers based on the similar sintering behavior and phase assemblages during reaction.[115] Others have found Ce to be a good surrogate for pyrochlore materials when the synthesis of the material took place in an oxidizing atmosphere and acceptable for zirconia-based ceramics; however, the use of Ce as a surrogate in zircon-based ceramics was considered limited.[116] Despite conflicting

reports on the applicability of Ce as a surrogate for Pu, it is still widely used in simulated waste forms.

The incorporation of Ce into zirconolite materials has been studied previously. Vance and coworkers[117] synthesized zirconolite materials in a reducing atmosphere and found that Ce could be successfully substituted onto the calcium site as a trivalent ion in small quantities, $Ca_{0.8}Ce_{0.2}ZrTi_{1.8}Al_{0.2}O_7$, when using aluminum as a compensating ion. When tetravalent Ce was targeted on the zirconium site ($CaZr_{0.8}Ce_{0.2}Ti_2O_7$), two zirconolites were reported to be formed, with one polymorph containing a majority of the Ce. No valence data was reported.

In 1997, Begg[53] reported formation of two zirconolites when targeting tetravalent Ce on the zirconium site ($CaZr_{0.8}Ce_{0.2}Ti_2O_7$). The synthesis of these materials was performed in air as opposed to the reducing atmosphere used in Vance's experiments.[117] The new zirconolite phase that was formed belonged to the 4M (monoclinic) polymorph as opposed to the 2M polymorph.

2M-ziconolite has been described by Rossel[33] as having an anion deficient fluorite structure with layers of corner sharing TiO_6 octahedra that are separated by layers containing ZrO_7 and CaO_8 polyhedra. This polymorph forms with compositions of $CaZr_xTi_{3-x}O_7$ with $0.8 < x < 1.37$. The 4M-zirconolite is described by Coelho[48] as having an enlarged unit cell (~22Å compared to ~11Å of 2M) due to the cation occupancy. There are two full occupancy Ti sites in the 2M structure, opposed to only one full occupancy Ti site in the 4M structure, requiring a doubling of the c axis to accommodate. The 4M-zirconolite is formed when cations (such as Nd used by Coelho[48]) substitutes on both the calcium and zirconium sites simultaneously with 0.5-0.8 formula units creating an alternate layering of the structure. The structures are compared in Figure V-1.

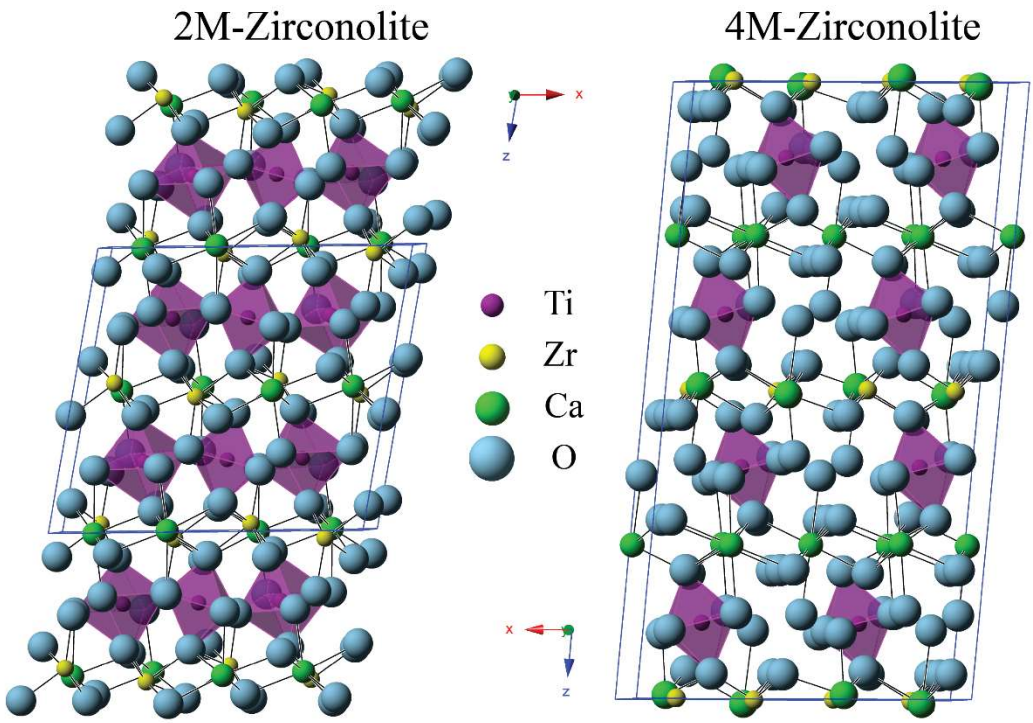

Figure V-1. 2M and 4M polymorphs of zirconolite, showing only the fully occupied Ti sites.

In addition to the previously mentioned studies, the incorporation of cerium into zirconolite and related pyrochlore structures has been investigated by many other research groups, both experimentally and theoretically.[55,118-121] The tendency of Ce to take on both tri- and tetravalent states leads to the formation of ancillary phases when targeting a single phase, such as perovskite and cerianite[54] and sphene and perovskite.[122]

V.2. Methodology

V.2.1 Atomistic Modeling

Atomistic modeling can aid in the understanding of the Ce incorporation into materials for nuclear waste immobilization. Pyrochlore materials have been studied using different modeling methods.[123-125] In general, an energy minimization technique is used with Buckingham potentials to obtain a relaxed structure. One program that utilizes this technique is General Utility Lattice Program (GULP). This program takes the internal energy (which is made up of coulombic, polarizability, dispersion, etc.) and writes it as a Taylor series, calculates the derivative (g) and the second derivative (H), and uses the

equation $\Delta x = -H^{-1}g$ to find the path towards the local minimum. The second derivative is in matrix form, and calculating the inverse of this matrix is the most time consuming step, and therefore is only done after a set number of calculations.[126]

Defect calculations are then performed to find the defect energies of the Ce substitutions using the Mott-Littleton technique.[127] This technique utilizes two regions surrounding the defect to calculate the energy and is illustrated in Figure V-2. The defect is located in the center, or midpoint between multiple defects. Regions are specified by radii, to include an appropriate amount of ions. Ions in Region I are strongly affected by the defect and are relaxed explicitly using energy minimization and force balance techniques. Ions in Region II are weakly perturbed and the atom positions are approximated. A larger Region I allows for more complete relaxation around the defect. The defect energy is calculated by taking the difference in energy between perfect regions and the defective regions.

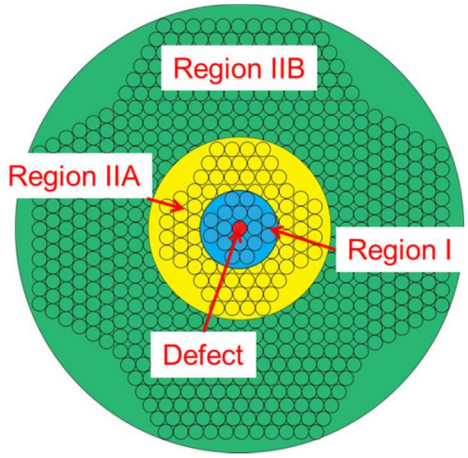

Figure V-2. Illustration of the regions surrounding a defect in the Mott-Littleton technique.

V.2.2 Phase Content Determination in Zirconolite Materials

Powdered materials were analyzed with X-ray diffraction (XRD) with a D8 Advance instrument (Bruker) over a range of 15-115 °2θ with a step size of 0.03°2θ and a count time of 1s using a Lynxeye position-sensitive detector. The pattern was evaluated with Rietveld analysis using the program TOPAS (Bruker). The XRD patterns were fitted to $CaZrTi_2O_7$ (2M-zirconolite), $CaZrNdTi_2O_7$ (4M-zirconolite), and $Ca_{0.4}La_{0.4}TiO_3$

(perovskite) with PDF cards #04-002-4312, 04-009-5863, and 00-055-0841, respectively. The relative phase amounts of the materials were calculated from the Rietveld scale factors.

V.2.3 High Temperature X-ray Diffraction (HTXRD)

Phase conversion after SPS was studied using HTXRD using a Siemens D5000 diffractometer equipped with a custom high temperature stage.[128] A SPS sample of $CaZr_{0.6}Ce_{0.4}Ti_2O_7$ composition was powdered and mounted on an alumina sample holder by mixing with isopropanol. Table V-1 shows two time-temperature profiles that were used to investigate the phase conversion.

Table V-1. HTXRD Schedules Used to Study Phase Conversion of Ce-Zirconolite Post-SPS

Schedule	Ramp Rate (°C/min)	Max Temperature (°C)	Hold Time (hr)	Scan Rate at T (scan/hr)
1	30	1300	1	3
2	30	1350	6	2

V.2.4 X-ray Absorption Near Edge Spectroscopy (XANES)

The valence state of Ce in zirconolite and pyrochlore samples was determined with XANES performed at the Cornell High Energy Synchrotron Source (CHESS). The Ce L_{III}-edge was measured in fluorescence at room temperature. The scans were collected in 0.25 eV steps from 5685-5785 eV. The amounts of tri- and tetravalent Ce present was determined by a linear relationship between the edge energies of CeO_2 (99.99%, Alfa Aesar) and $CePO_4$ (99%, Alfa Aesar) powders used as standards.

V.3. Result and Discussion

V.3.1 Defect Calculations

The structures were first relaxed using Buckingham potentials for the element-oxygen interactions found in the literature. The values of the lattice constants and density from the literature and after relaxation using GULP are listed in Table V-2.

Table V-2. Values of Lattice Constants and Densities for Zirconolite and Pyrochlore Materials Found in the Literature and After Structural Relaxation Using GULP

Property	$CaZrTi_2O_7$		$Nd_2Ti_2O_7$	
	Experimental[33]	**Calculated**	**Experimental[129]**	**Calculated**
Lattice Volume	1014.06	1016.17	539.24	541.61 (4.4)
a (Å)	12.4458	12.93 (3.9)	7.6747	7.56 (-1.5)
b (Å)	7.2734	7.13 (-2.0)	13.0025	13.21 (1.6)
c (Å)	11.3942	11.29 (-0.9)	5.640	5.47 (0.2)
β or γ (°)	100.533	102.4 (1.9)	98.517	98.2 (-0.3)
ρ (g/cm^3)	4.4418	4.433 (-2.1)	6.110	6.09 (-0.4)
*percent variation in parentheses				

The heat of solution was calculated by computing the lattice energies of the structures and the energy of the defects in the equation. The lower the heat of solution, the more likely the substitution is to occur. Six and five possible substitution mechanisms for Ce into zirconolite and pyrochlore listed in Table V-3 and Table V-4 respectively. Note that different Buckingham potential parameters were used whether Ce was present as tri- or tetravalent. The most likely substitutions according to these defect calculations are Ce substitution on the zirconium site (zirconolite, Table V-3) and trivalent Ce substitution on the Nd site (pyrochlore, Table V-4). Defect energies were calculated for different combinations of atomic sites.

Table V-3. Possible Substitution Mechanisms for Ce Incorporation into $CaZrTi_2O_7$

Substitution Mechanism	**Heat of Solution (eV)**
$2CeO_2 \rightarrow 2Ce_{Ca} + 2CaO + V_{Zr} + ZrO_2$	4.66
$CeO_2 \rightarrow Ce_{Zr} + ZrO_2$	0.01
$3CeO_2 \rightarrow 3Ce_{Ca} + 6CaO + 3V_{Ca}$	8.35
$CeO_2 \rightarrow Ce_{Ca} + CaO + O_i$	6.94
$2CeO_2 \rightarrow 2Ce_{Ca} + 2CaO + V_{Ti} + TiO_2$	5.99
$Ce_2O_3 \rightarrow Ce_{Ca} + Ce_{Zr} + CaO + ZrO_2$	3.90

Table V-4. Possible Substitution Mechanisms for Ce Incorporation into $Nd_2Ti_2O_7$

Substitution Mechanism	**Heat of Solution (eV)***			
$4CeO_2 \rightarrow 4Ce_{Nd} + V_{Ti} + 2Nd_2O_3 + TiO_2$	16.78	14.74	20.62	10.91
$CeO_2 \rightarrow Ce_{Ti} + TiO_2$	8.74		8.74	
$3CeO_2 \rightarrow 3Ce_{Nd} + V_{Nd} + 2Nd_2O_3$	6.59	5.85	10.25	2.183
$Ce_2O_3 \rightarrow 2Ce_{Nd} + Nd_2O_3$	2.22		-0.04	
$2CeO_2 + Al_2O_3 \rightarrow 2Ce_{Nd} + 2Al_{Ti} + 2TiO_2 + Nd_2O_3$	13.66	12.72	15.66	10.73
*various combinations of defects on atomic sites				

V.3.2 Cerium Incorporation in Zirconolite Materials

Figure V-3 shows the XRD patterns of zirconolite samples with Ce substitution from x = 0-0.5, targeting the zirconium site. The amount of 4M-zirconolite (compared to 2M-zirconolite) is seen to increase with greater Ce content. Rietveld analysis confirms this trend and the results are listed in

Table V-5. By x = 0.5, the zirconolite is present as the 4M polymorph. A small amount of perovskite ($Ca_{0.4}Ce_{0.4}TiO_3$) is also seen in all these samples. This is most likely due to the substitution of Ce on the calcium sites, making excess calcium available to react contrary to the formulation.

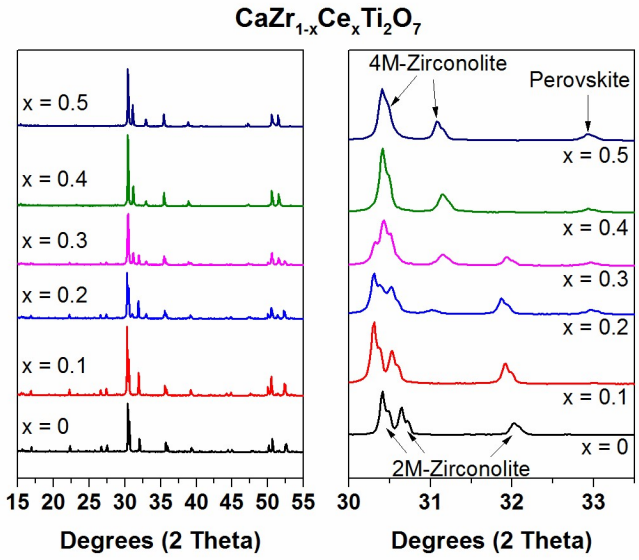

Figure V-3. XRD patterns of Ce-zirconolites.

Table V-5. Percentages of Phases Present in Zirconolite Powder Samples Synthesized Via Solid-State Sintering Determined by Rietveld Analysis

Sample	**2M-Zirconolite**	**4M-Zirconolite**	**Perovskite ($Ca_{0.4}Ce_{0.4}TiO_3$)**
$CaZr_{0.9}Ce_{0.1}Ti_2O_7$	99.0(1) wt%	0 wt%	0.9(1) wt%
$CaZr_{0.8}Ce_{0.2}Ti_2O_7$	74.5(3) wt%	19.3(3) wt%	6.2(1) wt%
$CaZr_{0.7}Ce_{0.3}Ti_2O_7$	45.6(3) wt%	49.0(3) wt%	5.4(1) wt%
$CaZr_{0.6}Ce_{0.4}Ti_2O_7$	3.6(3) wt%	89.4(3) wt%	6.9(2) wt%
$CaZr_{0.5}Ce_{0.5}Ti_2O_7$	0 wt%	95.6(4) wt%	4.3(3) wt%

A representative SEM image of synthesized $CaZr_{0.7}Ce_{0.3}Ti_2O_7$ taken in backscattered electron (BSE) mode is displayed in Figure V-4. Two phases can clearly be distinguished and are evenly distributed, which is in agreement with XRD of roughly equal amounts of 2M- and 4M-zirconolite. The contrast in backscattered images suggests that the one polymorph contains a greater amount of Ce. This is confirmed with EDS, with roughly twice as much Ce content in the bright phase. The bright phase belongs to 4M-zirconolite because as the amount of substituted Ce increases, the amount of 4M-zirconolite also increases. Therefore, the darker phase belongs to 2M-zirconolite. The EDS also shows that the dark phase (2M-zirconolite) is richer in Zr, indicating that greater portioning of Ce to the Zr site in 4M-zirconolite occurs.

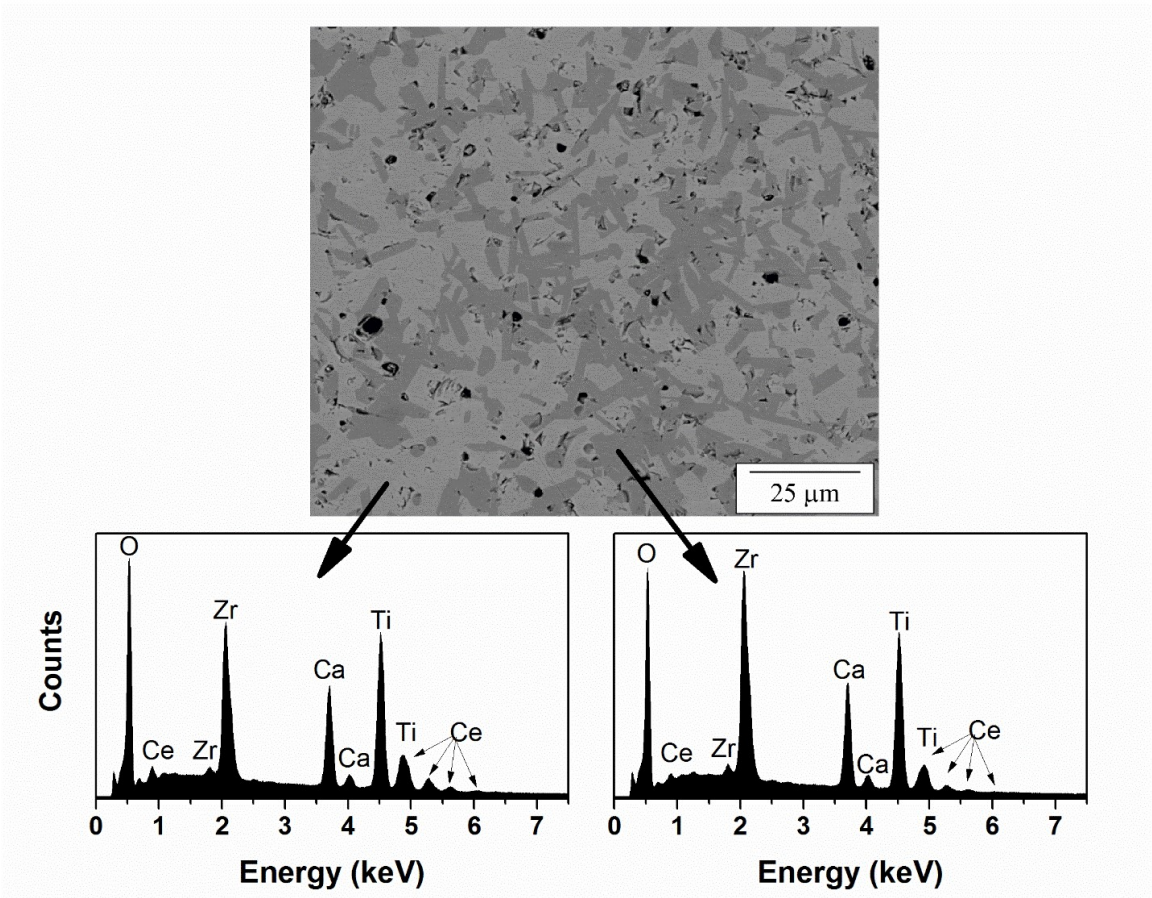

Figure V-4. Representative BSE image of synthesized $CaZr_{0.7}Ce_{0.3}Ti_2O_7$ and corresponding EDS spectra from the two phases detected.

XANES was performed on powdered samples of $CaZr_{0.5}Ce_{0.5}Ti_2O_7$ to detail the Ce valence state in these Ce zirconolites. The valence state of the Ce did not vary with composition, so only results from the x=0.5 composition are shown in this paper. Figure V-5 shows the XANES results from the standards, CeO_2 and $CePO_4$, and the synthesized powder. From the relationship between the edge energies, the synthesized powders contain about a 50/50 mix of tri- and tetravalent Ce. The presence of both tri- and tetravalent Ce demonstrates the ability of Ce to reduce at high temperatures in oxidizing atmospheres.[53] Trivalent Ce can co-substitute on both the Ca and Zr sites (as is seen in the 2M-zirconolite), and the tetravalent Ce can substitute for Zr (as in the 4M-zirconolite) without a need for a compensating ion. In zirconolite, this is often achieved by substituting Al for Ti.[53,130]

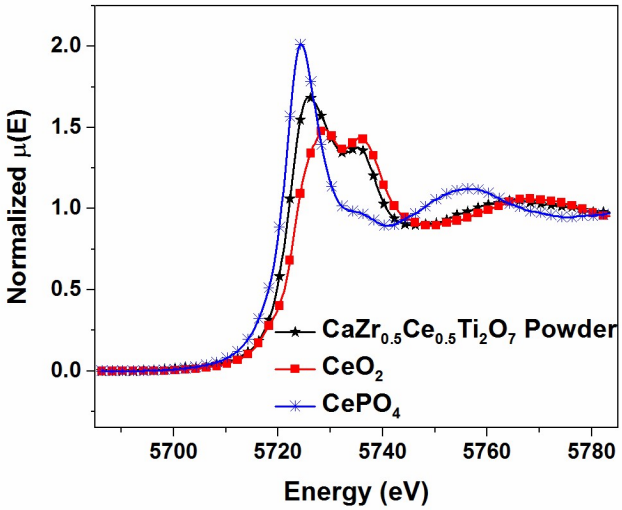

Figure V-5. XANES results from standard materials and synthesized Ce-zirconolite powder.

V.3.3 SPS of Ce-Zirconolites

To consolidate the powder into monoliths, SPS was performed on the Ce-zirconolites. The sintering behavior of $CaZr_{0.9}Ce_{0.1}Ti_2O_7$ was very similar to that of single phase material, where rapid consolidation occurs immediately prior to reaching maximum temperature. XRD of the resulting pellet shows similar phases to starting powder with a small amount of perovskite phase (Figure V-6). The sintering peak of $CaZr_{0.6}Ce_{0.4}Ti_2O_7$ was 'sharper' than the single phase material, indicating more rapid sintering. XRD of the resulting pellet shows an increase of perovskite phase. The change in sintering behavior is attributed to the sintering of both zirconolite and perovskite. The sintering curve and XRD are also shown in Figure V-6. The destabilization of 4M-zirconolite in favor of 2M-zirconolite after sintering should also be noted.

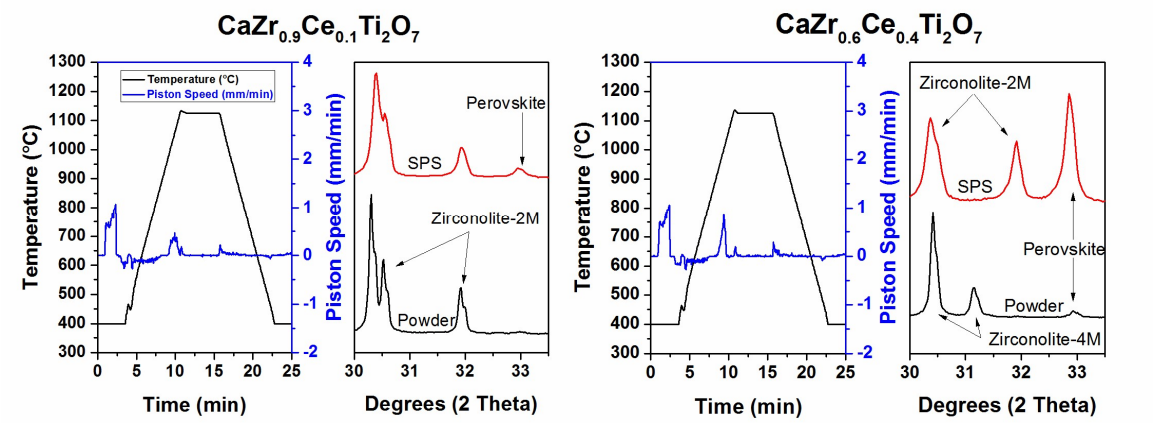

Figure V-6. Temperature profile and piston speed during SPS of $CaZr_{0.9}Ce_{0.1}Ti_2O_7$ and $CaZr_{0.6}Ce_{0.4}Ti_2O_7$ including XRD comparison of the powder and resulting SPS pellet.

This result demonstrates that the conversion to perovskite is a fast process and it occurs below the sintering temperature of zirconolite. SPS was performed on the range of Ce-substituted zirconolites. It was found that the amount of perovskite formed during SPS increases as the amount of Ce in the material increases. A comparison of the XRD patterns of the sintered Ce-substituted zirconolites is shown in Figure V-7. The stabilization of a perovskite phase from zirconolite in reducing conditions (as in the case of SPS) has been reported previously.[117,131] XANES reveals that about 90% of the Ce is present in the trivalent state after SPS (Figure V-7). Zirconolite transformation into perovskite is due to the partial reduction of Ti^{4+} to Ti^{3+} in the zirconolite structure.[131] In order for charge compensation to occur in the zirconolite structure, Zr relocates to the Ca site, allowing excess Ca and Ti to react to form perovskite with the reduced Ce.

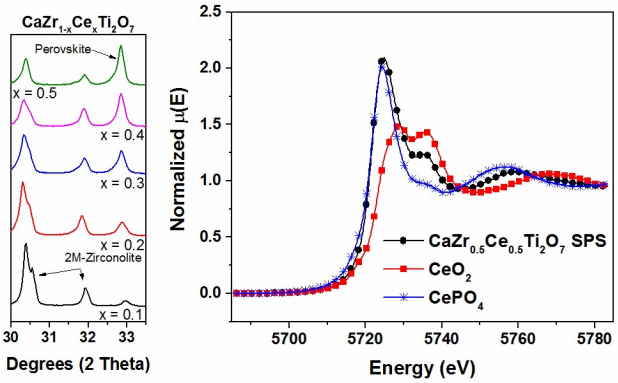

Figure V-7. XRD comparison of SPS Ce-substituted zirconolites along with XANES results showing a majority of trivalent Ce.

V.3.4 Phase Conversion of Ce-Zirconolites

The formation of perovskite during SPS is undesirable due to the superior chemical durability of zirconolite[46] compared to the perovskite phases. Thus, a heat treatment in air after SPS is required to convert the perovskite back into zirconolite. HTXRD was used to monitor the phase conversion during heat treatment. Schedule 1 (Table V-1) reveals that $CaCeTi_2O_7$ forms as an intermediate phase at temperatures up to 1300°C, as seen in the XRD patterns in Figure V-8. 4M-zirconolite does not form in the $CaZr_{0.6}Ce_{0.4}Ti_2O_7$ sample during Schedule 1. No significant changes to the patterns were seen in the subsequent measurement at 1300°C.

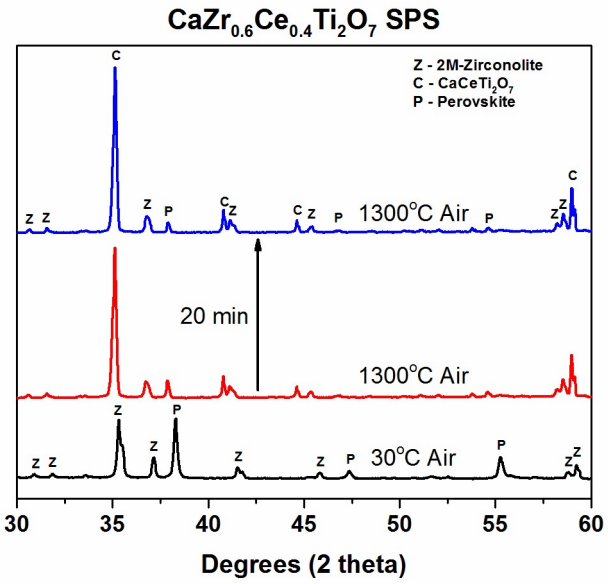

Figure V-8. *in situ* XRD patterns of $CaZr_{0.6}Ce_{0.4}Ti_2O_7$ at 1300°C showing the conversion of perovskite into $CaCeTi_2O_7$.

A second HTXRD schedule was performed to eliminate the $CaCeTi_2O_7$ that forms as an intermediate phase. At 1350°C, $CaCeTi_2O_7$ and 2M-ziconolite are converted into 4M-zirconolite (Figure V-9). Rietveld analysis was performed on these patterns to determine the phase contents of the specimen during the 4M-zirconolite formation. Select diffraction patterns and the corresponding wt% determined by Rietveld analysis are shown in Figure V-9. It can be seen that perovskite reacts to form $CaCeTi_2O_7$ at temperatures below 1350°C. During the 5 hour hold at 1350°C, the perovskite content reaches a plateau at around 9 wt%. The $CaCeTi_2O_7$ and 2M-zirconolite react during the first 2 h of the hold at 1350°C to form 4M-zirconolite which plateaus by around 3.5 h. The reaction did not go to completion (100% 4M –zirconolite) during the HTXRD experiment.

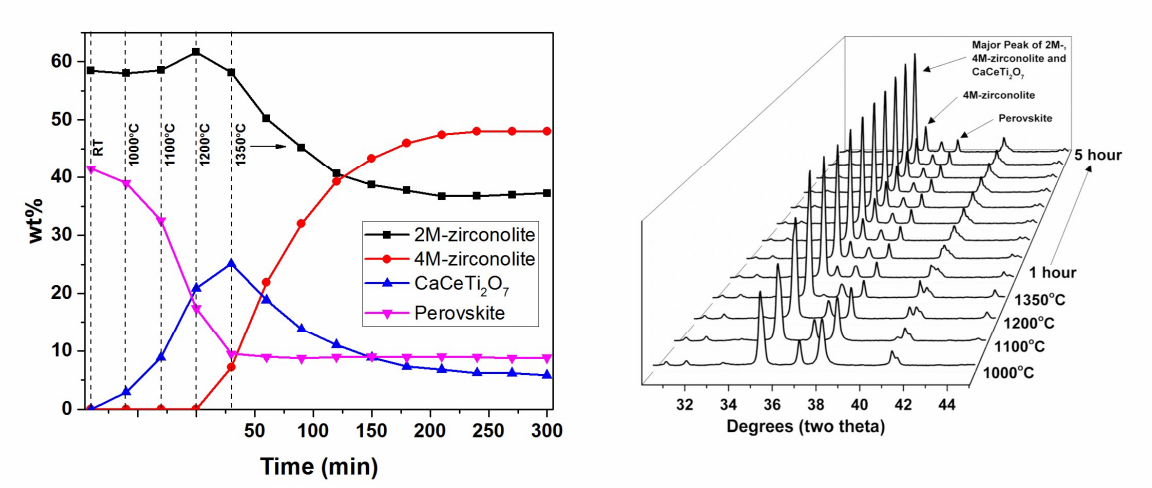

Figure V-9. Phase amounts and corresponding XRD patterns during heating and isothermal hold at 1350°C of $CaZr_{0.6}Ce_{0.4}Ti_2O_7$.

Conversion of the phases after SPS back to nearly the original phase composition was achieved by a furnace heat treatment at 1350°C for 24h. The longer heat treatment completes the conversion of $CaCeTi_2O_7$ into zirconolite (both 2M and 4M), which is desirable for the intended application. XRD patterns representing the phase changes are shown in Figure V-10.

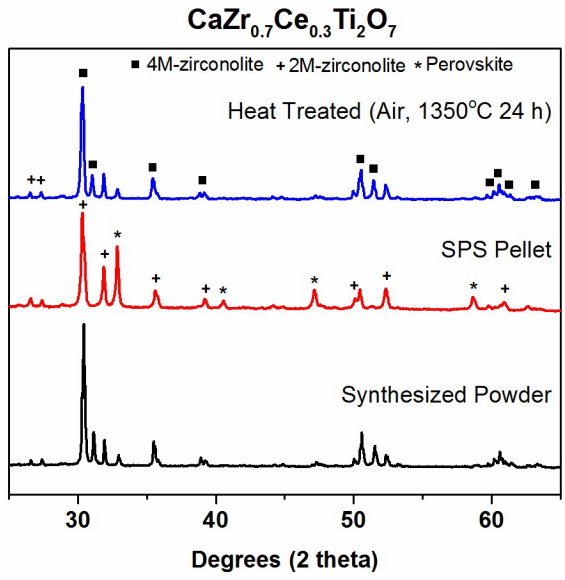

Figure V-10. XRD patterns comparing the phase assemblage in $CaZr_{0.7}Ce_{0.3}Ti_2O_7$ under different processing conditions.

V.3.5 Ce-Pyrochlore Synthesis and SPS

XRD reveals phase pure $Nd_2Ti_2O_7$ is obtained when Ce is substituted for Nd up to 25 mol % indicating that Ce is incorporated into the pyrochlore structure. The XRD patterns for these materials are shown in Figure V-11. The peaks systematically shift to lower two theta, indicating an increase in unit cell volume. XANES measurements (Figure V-11) show that nearly all Ce becomes trivalent after synthesis. This allows for the Ce to enter the pyrochlore structure without creating vacancies via charge balance. Instability of tetravalent Ce at high temperatures, even in oxidizing environments, is demonstrated.[115]

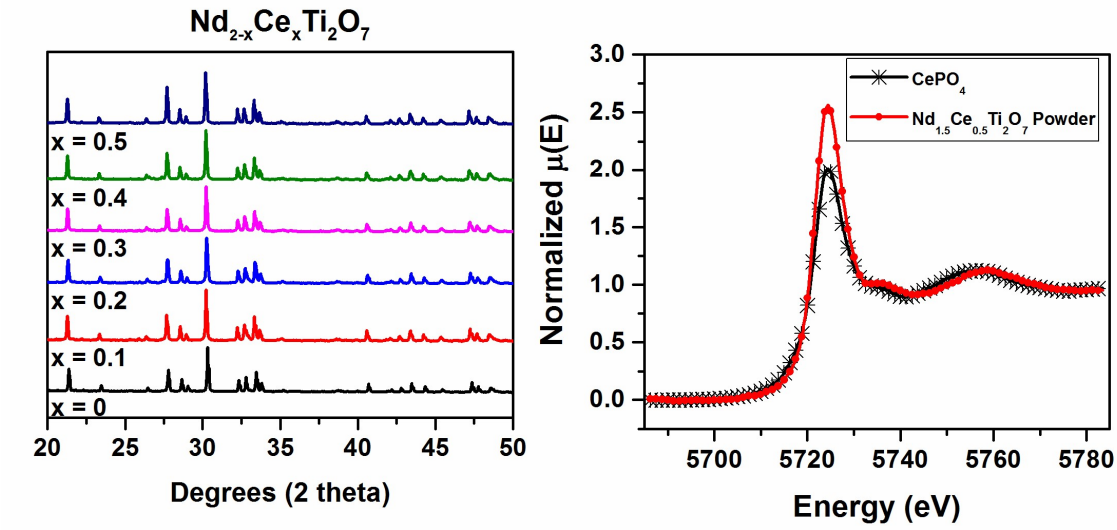

Figure V-11. XRD patterns of Ce substituted $Nd_2Ti_2O_7$ (right) and XANES spectra showing all trivalent Ce present in the sample (left).

The sintering behavior of the materials with varying amounts of Ce content is displayed in Figure V-12 by plotting the theoretical density as a function of time. The sintering time is short, increasing in theoretical density from ~65% to 98% in about 90 s before reaching the maximum temperature of 1225°C. Sintering behavior does not change with increasing Ce content, indicating that the sintering mechanism remains the same. The materials remain at elevated temperatures during sintering for > 600 s, which is important for the processing of nuclear waste forms.

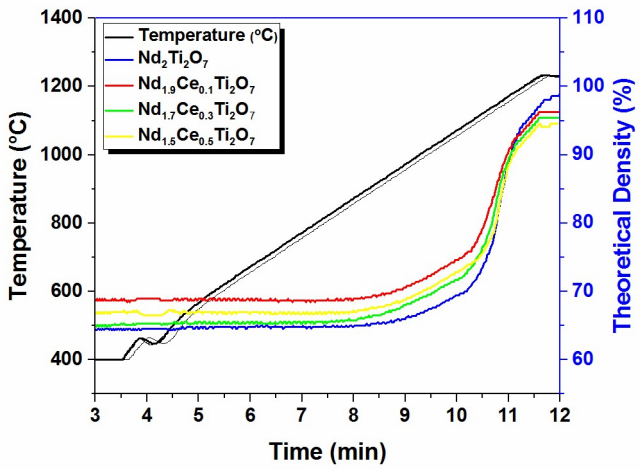

Figure V-12. Sintering behavior of Ce substituted $Nd_2Ti_2O_7$ during SPS.

V.4. Conclusions

Ce incorporation into the zirconolite structure was confirmed using XRD and supporting data from SEM/EDS and XANES. A transition from the 2M polymorph to the 4M polymorph with increasing Ce substitution is evident. In 2M-zirconolite, trivalent Ce co-substitutes on both the Ca and Zr sites, while both trivalent (Ca and Zr sites) and tetravalent (Zr sites) Ce substitutes into 4M-zirconolite. Conversion of 4M-zirconolite to perovskite and 2M-zirconolite occurs during the SPS process due to the reducing environment. This is due to the reduction of Ce^{4+} into Ce^{3+}, where the 2M-zirconolite is charge balanced by co-substitution of Ce^{3+} on the Ca and Zr sites and the perovskite forms due to the partial reduction of Ti^{4+} to Ti^{3+} leaving excess Ca an Ti to react with the trivalent Ce to form perovskite. HTXRD was used to study the transformation process of the perovskite into zirconolite in air. $CaCeTi_2O_7$ forms as an intermediate phase up until 1300°C, and 4M-zirconolite begins at 1350°C. The re-oxidation of Ce^{3+} and Ti^{3+} to their tetravalent states allows the original phase assemblage to be attained. The transformation to 4M-zirconolite is slow, but complete conversion to the original phase assemblage is achieved with a 24h heat treatment in air. Ce was fully incorporated into the $Nd_2Ti_2O_7$ structure, with the reduction of Ce^{4+} to Ce^{3+} during synthesis. The sintering behavior via SPS was unaffected by Ce content in pyrochlore materials.

VI. SPARK PLASMA SINTERING BEHAVIOR OF $Nd_2Ti_2O_7$

Neodymium titanate is a candidate material for nuclear waste immobilization due to its ability to accomodate rare earth elements and actinides as substituting ions on the neodymium site. Consolidation of nuclear waste forms using SPS presents many advantages over alternative methods, most notably the shorter sintering times required to produce dense waste forms. The sintering mechanism was investigated via a direct method by sintering samples at 1050°C under a range of applied pressures. A stress exponent of ~1 was obtained, corresponding to a sintering mechanism of grain boundary sliding. The activation energy during the final sintering stage (> 90% TD) was found to be 95 kJ/mol. A grain size exponent of 3.1 was determined, revealing that the grain boundary sliding is accommodated by grain boundary diffusion.

VI.1. Introduction

Fast sintering times and lower sintering temperatures to obtain dense ceramics[86] and encapsulation of the material during sintering has led to the consideration of SPS as a consolidation method for nuclear waste forms. This would lead to limited volatilization of radioactive elements during the consolidation process. The SPS process has been well documented for a number of different materials.[132-135]

Characterizing the mechanisms active during SPS has presented a challenge for researchers.[136-138] Indirect characterization has been applied to materials[137,139] based on the method proposed by Bernard-Granger. This technique utilizes the creep rate derived equation, which is written as[140]:

$$\frac{1}{\mu_{eff}}\frac{1}{D}\frac{dD}{dt} = K\frac{e^{-\frac{Q_D}{RT}}}{T}\left(\frac{b}{G}\right)^p\left(\frac{\sigma_{eff}}{\mu_{eff}}\right)^n \quad \text{(VI-1)}$$

where t is time, μ_{eff} is the instantaneous modulus of the compacted powder, K is a constant, R is the gas constant, T is the temperature, Q_D is the activation energy of the mechanism controlling densification, b is the Burgers vector, G is the grain size, σ_{eff} is the instantaneous effective stress acting on the powder bed, n and p are the stress and grain size exponent respectively. The effective stress and effective modulus can be written as:

$$\sigma_{eff} = \frac{1-D_0}{D^2(D-D_0)}\sigma_{mac} \quad \text{(VI-2)}$$

and

$$\mu_{eff} = \frac{E_{th}}{2(1+\nu_{eff})} \frac{D-D_0}{1-D_0} \quad \text{(VI-3)}$$

respectively, where E_{th} is the Young's modulus of the fully dense material, ν_{eff} is the effective Poisson's ratio, D_0 is the green density of the powder at the start of the sintering procedure, D is the instantaneous density of the compact, and σ_{mac} is the macroscopic applied pressure. Using this procedure, different values of the stress exponent, n, that indicates which sintering mechanism is active, have been obtained for alumina.[137,141] The discrepancy between the n values is due in part to the need to calculate effective parameters used in the analysis. The effective values fluctuate with relative density, and the evolution of these parameters are dependent on the equations chosen to calculate them.[142] Table VI-1 displays the stress and grain size exponents associated with hot pressing sintering mechanisms.[143]

Table VI-1. Exponents Associated with Hot Pressing Sintering Mechanisms

Densification Mechanism	**Stress Exponent (n)**	**Grain Size Exponent (p)**
Viscous Flow	1	0
Lattice Diffusion	1	2
Grain Boundary Diffusion	1	3
Liquid Phase Sintering	1	3
Grain Boundary Sliding	1-2	1
Dislocation Induced Plasticity	≥3	0

A direct characterization technique has been applied to alumina to alleviate the discrepancies found in the indirect characterizations.[142,144,145] The procedure is simple and is performed by comparing the densification rate as a function of applied stress at a fixed density value, eliminating the need to calculate effective parameters. In this study, the direct characterization approach is applied to $Nd_2Ti_2O_7$ to investigate the sintering behavior of this material in regards to nuclear waste form applications.

VI.2. Methodology

VI.2.1 Spark Plasma Sintering Schedules

Samples were sintered using a heating and cooling rate of 100°C to maximum temperatures between 1025 and 1075°C (as read by a pyrometer facing the outer die wall), with a 600 s hold time at maximum temperature and applied pressures of 18, 54, or 98 MPa during the run. A blank run, consisting of just the graphite mold and foil, with identical sintering parameters to each sample sintered was performed to subtract any background piston movement due to the die and foil. Samples for grain size measurement were produced by holding at 1050°C for 0.17, 0.5, and 1 h with 54 MPa applied pressure.

VI.2.2 Grain Size Measurement

The grain size of the sintered samples was evaluated using ASTM E112[146] to determine the grain size exponent. Section of the sintered pellets were polished down to 1 μm using a combination of SiC grit paper and diamond suspensions. Thermal etching was performed in a box furnace by ramping the temperature at 10°C/min to 1350°C, holding for 600 s, and cooling to room temperature at 10°C/min. Images were taken from 5 widely spaced areas on the polished and etched surfaces with scanning electron microscopy (SEM). The Heyn line-intercept method was used to then calculate the grain size.

VI.3. Results and Discussion

VI.3.1 Densification and Stress Exponent Determination

The evolution of the relative density during the 0.17 h isothermal hold can be seen in Figure VI-1. Applied pressures of 18, 54, and 98 MPa are compared, and the relative densities are similar across the three samples (~94% TD). This extends the viability of using the direct characterization method for these samples during the final sintering stage.

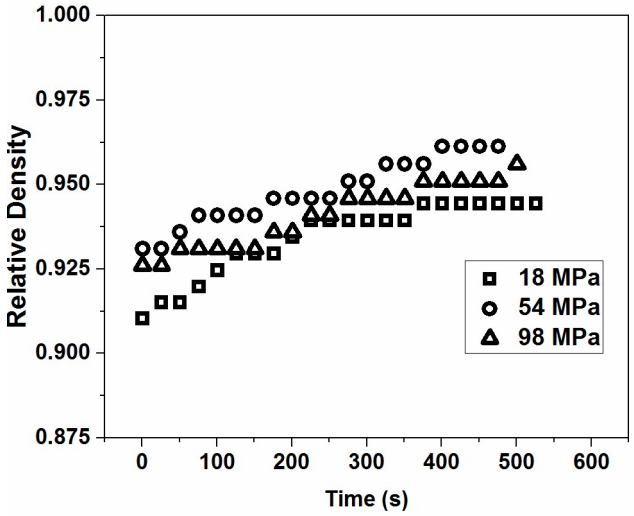

Figure VI-1. Evolution of relative density during SPS isothermal hold at 1050°C of $Nd_2Ti_2O_7$.

The densification rate during the isothermal hold time at 1050°C for these three samples is plotted against the applied pressure during the run in Figure VI-2. The corresponding linear fit gives a stress exponent (n) value of 1.06, which implies that the sintering mechanism active during the final stage of sintering is grain boundary sliding.[147]

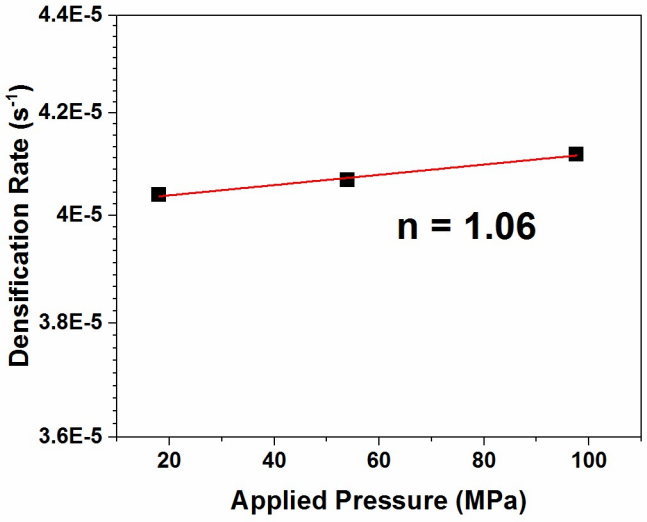

Figure VI-2. Densification rate as a function of applied pressure yielding a stress exponent (n) value of 1.06.

Additional experiments were performed to elucidate the sintering mechanism during the intermediate stage of sintering (< 90% TD), however the densities obtained during isothermal holds at temperatures lower than 1050°C were not consistent enough to apply the direct characterization method.

VI.3.2 Grain Size Exponent and Activation Energy

The grain size values for the samples sintered at 1050°C held at temperature for 600, 1800, and 3600 s with an applied pressure 54 MPa are plotted vs densification rate in Figure VI-3. The grain size increases as the hold time increases, typical when sintering ceramics.[148,149] The linear fit of this data yields a grain size exponent (p) of 3.1, corresponding to grain boundary diffusion.[150]

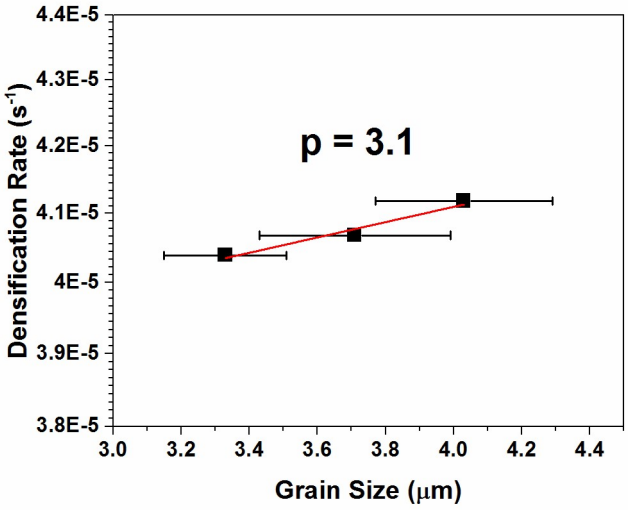

Figure VI-3. Densification rate versus grain size of $Nd_2Ti_2O_7$ SPS samples yielding a grain size exponent (p) value of 3.1.

To calculate the activation energy for the final sintering stage, samples were sintered at 1025, 1035, 1050, and 1075°C with 54 MPa applied pressure. Each of these samples are > 90% TD, remaining in the final sintering stage regime. A semi logarithmic Arrhenius plot of the densification rate as a function of inverse temperature was used and can be seen in Figure VI-4. The activation energy corresponding to the linear fit is 95 kJ/mol. This is a low value obtained for the activation energy of the sintering mechanism,

however, no activation energies have been reported for this material to compare the present values.

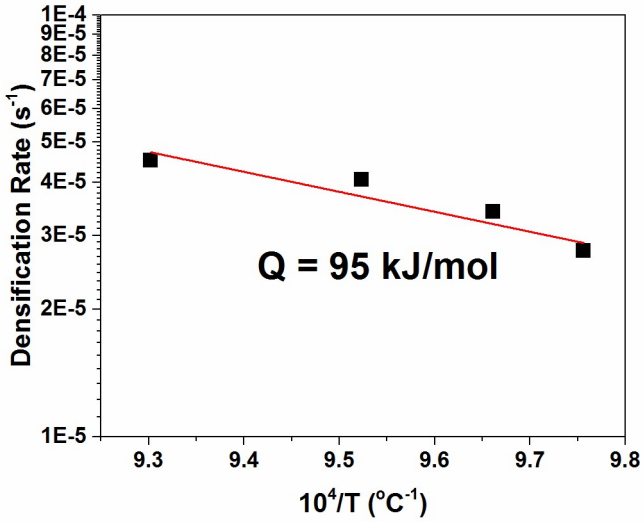

Figure VI-4. Semi-logarithmic Arrhenius plot of densification rate versus inverse maximum SPS temperature used to obtain the activation energy.

VI.4. Conclusion

The sintering mechanism of neodymium titanate pyrochlore during SPS was investigated using a direct characterization method. It was determined that the sintering mechanism during the final sintering stage (> 90% TD) is grain boundary sliding (stress exponent n = 1) accommodated by grain boundary diffusion (grain size exponent p = 3).

VII. PERFORMANCE TESTING OF SPARK PLASMA SINTERED ZIRCONOLITE AND PYROCHLORE

Chemical durability and resistance to irradiation damage are two important criteria commonly used to validate a material's applicability as a waste form. Compositions of Ce-substituted zirconolite and pyrochlore, $CaZr_{1-x}Ce_xTi_2O_7$ and $Nd_{2-x}Ce_xTi_2O_7$ with x = 0.1, 0.3 and 0.5, as described in Section V, were evaluated for their performance as waste form materials. In this study, chemical durability testing was performed using the product consistency test (PCT) and the Materials Characterization Center (MCC) monolithic leaching test. Ce leaching in these materials was low (2×10^{-5} g/m^{2}day) or below the detectable limit in some cases. Ion beam irradiations of compositions with x = 0.1 and 0.5 were performed using Kr^{3+} and He^{+} ions (simulating heavy and light ions respectively) to 0.5 displacements per atom (dpa). Complete amorphization is observed in all samples under heavy ion irradiation, while no structural changes are observed under light ion irradiation.

VII.1. Introduction

The chemical durability of nuclear waste form materials is of critical importance in defining the long-term storage performance. Various test methods have been proposed for studying the leaching behavior including the PCT,[151,152] the MCC standard,[122,153,154] and the vapor hydration test (VHT).[155-157]

Zirconolite materials have demonstrated high chemical durability under leaching conditions.[158-161] Cat *et al*.[50] produced an Nd-doped zirconolite via solid-state synthesis and performed the PCT, yielding a leach rate of Nd of 10^{-5}g/m^{2}d after 42 days Using the MCC-1 test, Wen *et al.*[51] showed the Ce leach rate in solid-state synthesized Ce doped zirconolite was 10^{-6} g/m^{2}d after 28 days. Pyrochlore materials also exhibit acceptable chemical durability for nuclear waste form applications.[160,162,163] One gadolinium titanate produced by self-propagating high-temperature synthesis (SHS), has a leaching rate of Gd of 2×10^{-4} g/m^{2}d after 42 days, determined using the MCC-1,[164] with similar results obtained for a gadolinium zirconate under the same leaching conditions.[165]

Radiation stability is also of crucial in the determination of a material's use as a nuclear waste form. Ion beam irradiation and self-irradiation[37,106,166] are the typical ways

to determine a materials radiation stability, characterized by XRD. The use of ion beams has been described in Section IV.1. Ion beams provide accelerated degradation results, and self-irradiation experiments provide accurate behavior of materials interacting with radioactive decay. When subjected to light ion irradiation (He^+) with fluences up to 10^{21} ions/m^2, zirconolite materials do not show amorphization via XRD and microstructural analysis.[167] Heavy ion irradiation (Kr^+, Xe^+, or Ar^+) result in the amorphization of both zirconolite and pyrochlore materials.[99,168,169]

VII.2. Methodology

VII.2.1 Leaching Tests

The PCT Method-A[151] was performed on compositions of $CaZr_{1-x}Ce_xTi_2O_7$ and $Nd_{2-x}Ce_xTi_2O_7$ with x = 0.1, 0.3 and 0.5 consolidated by SPS as described in Section V to assess chemical durability. Monolithic samples were ground to 100-200 mesh particle size, washed and prepared according to the standard procedure. Fifteen milliliters of Type-I ASTM water were added to 1.5 g of sample in stainless steel vessels. Samples were done in triplicate. The vessels were sealed and placed in an oven at 90 ± 2°C for 7 days. Once cooled, the resulting solutions were acidified and analyzed for cation concentrations using inductively coupled plasma – atomic emission spectroscopy (ICP-AES).

The Materials Characterization Center (MCC) standard[170] was performed using disks of compositions of x = 0.1 and 0.5 of zirconolite materials densified via SPS and x = 0.5 for pyrochlore materials. The samples had approximate surface areas of 150 mm^2 with each face ground to 600 grit with SiC paper. Samples were suspended from a stainless steel support by Pt wire inside a sealed stainless steel vessel with 15 mL of Type-I ASTM water. The vessels were placed in an oven at 90°C for 1, 7, 28, and 49 days. The experimental setups for the chemical durability tests is shown in Figure VII-1.

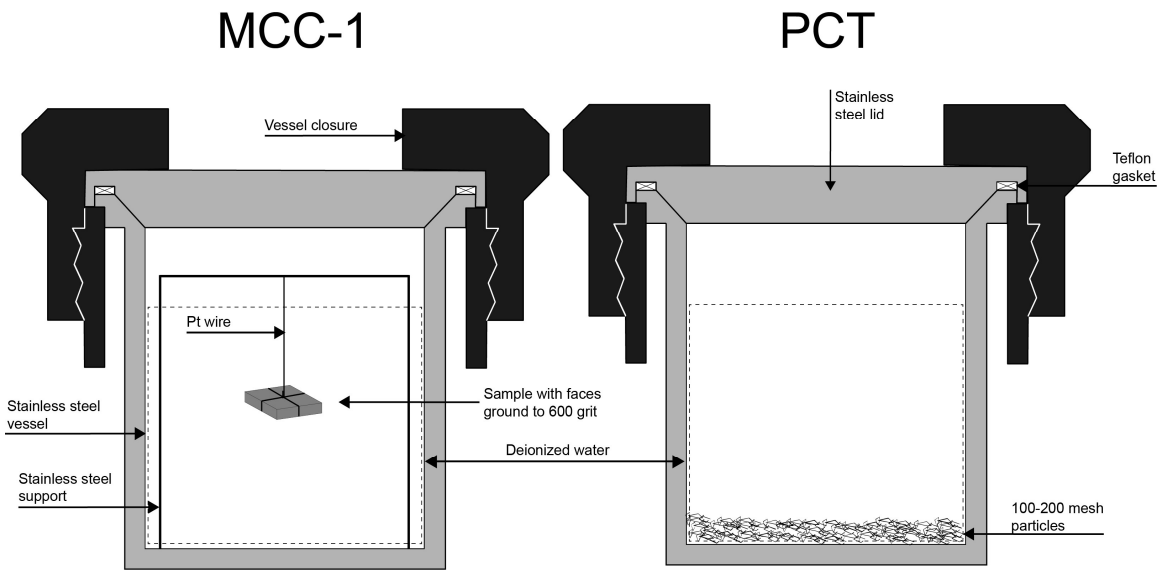

Figure VII-1. Schematic of the MCC-1 and PCT sample setup.

VII.2.2 Irradiation Tests

Samples for ion irradiation experiments were prepared by polishing a surface to 1 μm using a diamond suspension. The radiation dose in these materials was estimated using the SRIM program.[107] 380 keV He^{+} and 3 MeV Kr^{3+} implantations were performed on $CaZr_{1-x}Ce_xTi_2O_7$ and $Nd_{2-x}Ce_xTi_2O_7$ with x = 0.1 and 0.5 (Section V) using the IBL at the University at Albany. Samples received doses of 0.5 dpa of either He^{+} (2.8×10^{16} ions/cm) or Kr^{3+} (2.0×10^{14} ions/cm) ions. The energies of the He^{+} and Kr^{3+} ions were chosen to create damage depths of ~1 μm.

VII.2.3 Charaterization

Elemental concentrations of the leachates were determined concentrations using ICP-AES. The normalized release values are calculated using the following equation:

$$NR = \frac{C*V_l}{f*A_S*\Delta t} \quad \text{(VII-1)}$$

where NR is the normalized release of Ce, C (g/L) is the concentration of Ce in the leachate, V_l (m^3) is the volume of the leachate, f (wt%) is the fraction of the element in the unleached sample A_s (m^2) is the geometric surface area of the sample and Δt (d) is the duration of the leach testing. XRD was also performed to observe any phase changes that may have occurred during testing.

Irradiated surfaces were analyzed with GIXRD by scanning 2θ values from 10 to 60° with a step size of 2θ value of 0.04° and a dwell time of 40 s at an angle of incidence of 2 degrees. Scans were made on samples before and after irradiation to compare changes that occurred during irradiation.

VII.3. Results and Discussion

VII.3.1 Chemical Durability Results and Analysis

Ce-substituted zirconolite and pyrochlore were found to be extremely leach resistant according to PCT and MCC-1 methods. All zirconolite materials subjected to the MCC-1 procedure released no Ce above the detection limit of the instrument (< 2.00 µg/L) demonstrating high chemical durability under these conditions. Under PCT conditions, only the lowest Ce content zirconolite, $CaZr_{0.9}Ce_{0.1}Ti_2O_7$, released any Ce during testing. This result indicates that the 4M-zirconolite polymorph is more chemically durable than the 2M-zirconolite polymorph.

Results of the MCC-1 testing of $Nd_{1.5}Ce_{0.5}Ti_2O_7$ revealed that Ce was released during the 1 and 7 day tests (Table VII-1). The amount of Ce released decreased between the 1 and 7 day tests, and decreased below the instrument's detectable limit for the 28 and 49 day tests. Ce-substituted pyrochlore materials under PCT conditions confirmed high chemical durability, as only the highest Ce content pyrochlore released Ce above the detectable limit. The leachate results for the chemical durability testing are summarized in Table VII-1.

Table VII-1. Normalized Ce Release Rates of Various Ceramics

Composition	**Test – Duration (days)**	**Normalized Release ($g/m^2day \times 10^{-5}$)**	**Reference**
$CaZr_{0.9}Ce_{0.1}Ti_2O_7$	PCT – 7	0.132	This work
$Nd_{1.5}Ce_{0.5}Ti_2O_7$	PCT – 7	0.202	This work
	MCC-1 – 1	66.147	
	MCC-1 – 7	3.967	
	MCC-1 – 21	–	
$Zr_{1-x-y}Ce_xNd_yO_{2-y/2}$ (x = 0.05-0.25, y= 0.15-0.75)	MCC-1 – 1	~ 15 – 35	[171]
	MCC-1 – 7	~ 5 – 15	
	MCC-1 – 21	~ 1 – 5	
$CaZr_{0.71}Ce_{0.25}Ti_{1.89}Si_{0.15}O_7$-$Ca_{0.61}Ce_{0.17}Si_{0.96}Ti_{1.04}O_5$-$Ca_{0.88}Ce_{0.05}Ti_{0.98}Si_{0.03}O_3$ (56.7-22.7-20.6 vol%)	MCC-1 – 1	~ 30	[122]
	MCC-1 – 7	~ 10	
	MCC-1 – 21	~ 1	
$Gd_{1.5}Nd_{0.5}Zr_{1.5}Ce_{0.5}O_7$	PCT – 7	~ 0.3	[172]
$xCeO_2$-(100-x)($40Fe_2O_3$-$60P_2O_5$), x = 2, 4, 6, 8, glass-ceramic	PCT – 7	~ 5	[76]

Table VII-1 details chemical durability tests performed on various ceramic materials and the corresponding normalized Ce leach rates. The ceramics tested in this thesis demonstrate superior Ce leachability compared to other ceramics under similar testing conditions.

XRD results show that no phase changes occur during PCT or MCC-1 testing. Figure VII-2 shows XRD patterns of $CaZr_{0.9}Ce_{0.1}Ti_2O_7$ and $CaZr_{0.5}Ce_{0.5}Ti_2O_7$ before and after the PCT treatment. The decreased intensity of the treated samples is due to the limited amount of material available to scan.

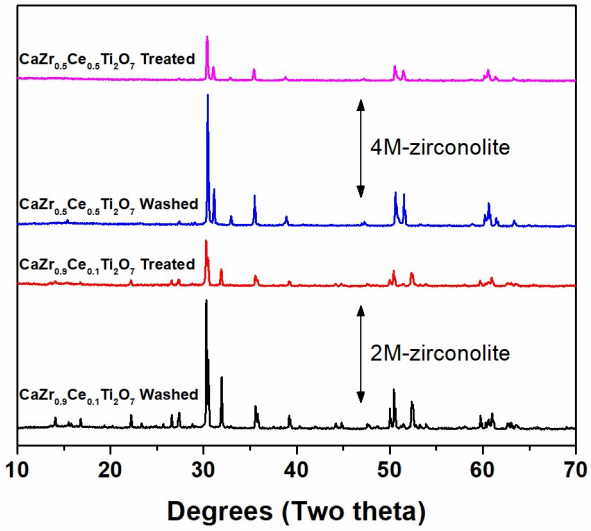

Figure VII-2. XRD patterns of Ce-zirconolite materials before and after PCT.

VII.3.2 Irradiation Resistance

GIXRD patterns of Ce-substituted materials are shown in Figure VII-3 and Figure VII-4. Under light ion irradiation, a decrease in peak intensity can be seen, but no new peaks appear after treatment in either high or low content Ce samples. Irradiations with heavy ions caused nearly complete amorphization, only a small number of peaks could be seen above the amorphous hump in zirconolite samples. The amount of Ce substituted into the zirconolite and pyrochlore structures does not affect the extent of irradiation damage in these samples. These results presented here support the results seen in multiphase samples described in Section IV where the non-hollandite phases remained relatively unaffected by light ion irradiation and were amorphized by heavy ion irradiations.

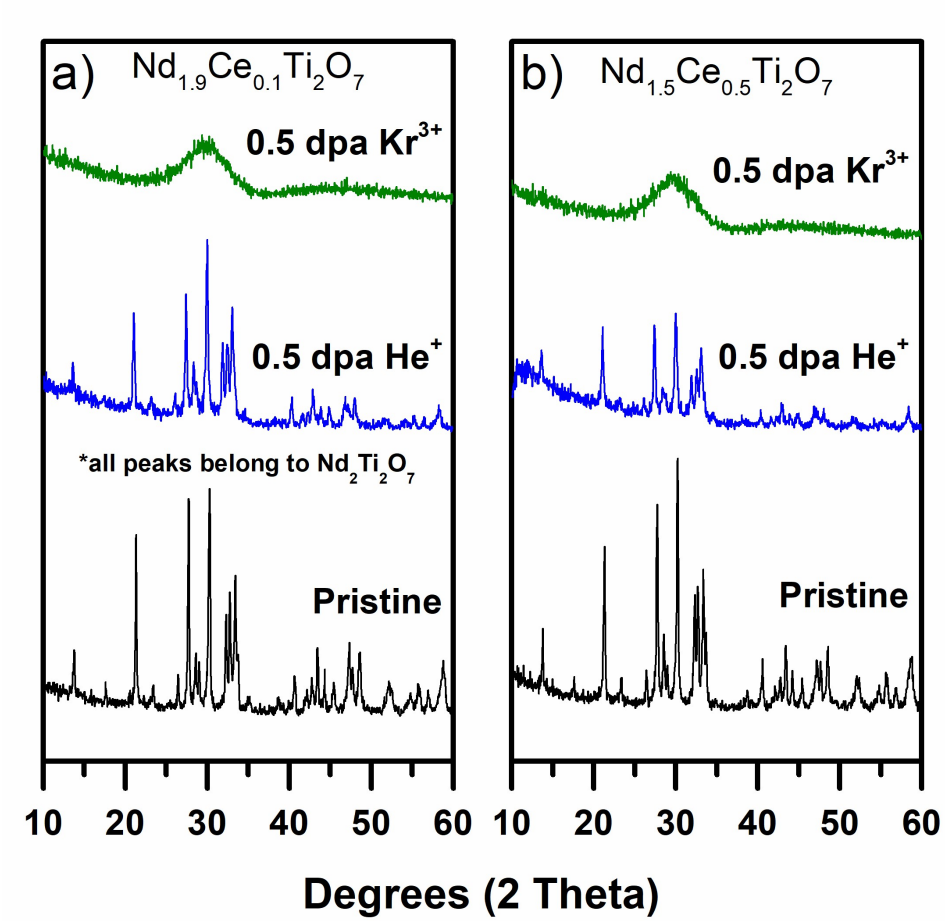

Figure VII-3. GIXRD patterns of $Nd_{1.9}Ce_{0.1}Ti_2O_7$ and $Nd_{1.5}Ce_{0.5}Ti_2O_7$ samples consolidated by SPS before and after 0.5 dpa He^+ or Kr^{3+} irradiations.

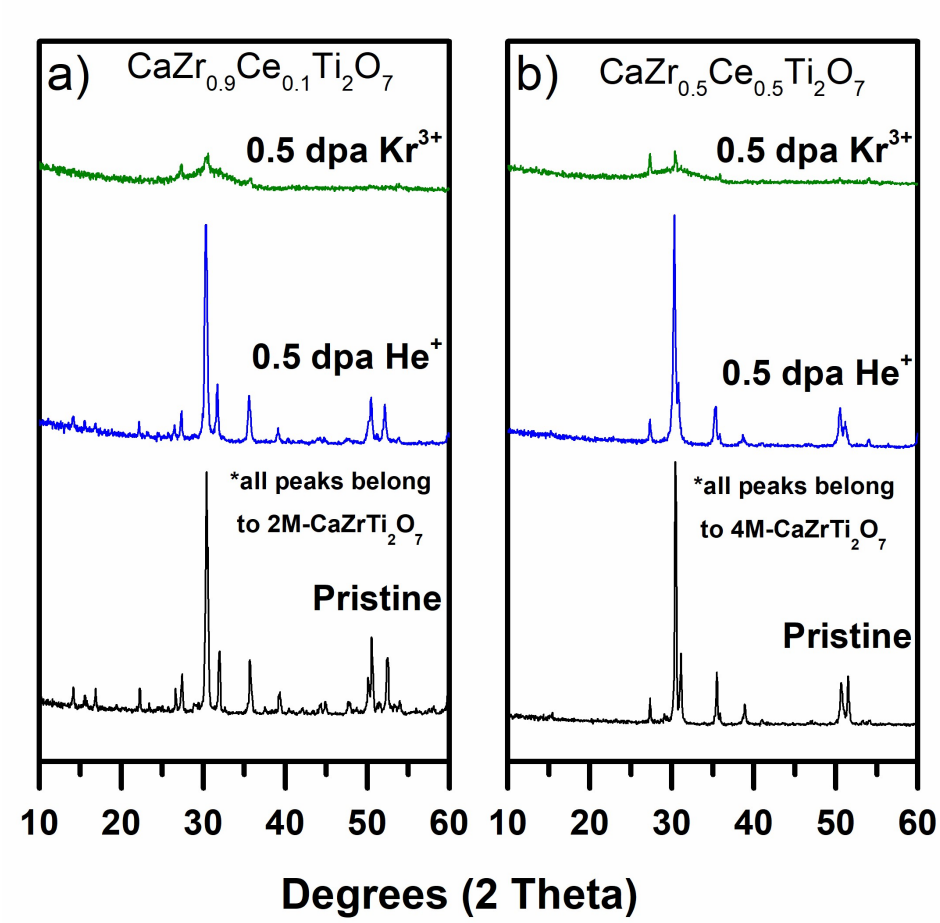

Figure VII-4. GIXRD patterns of $CaZr_{0.9}Ce_{0.1}Ti_2O_7$ and $CaZr_{0.5}Ce_{0.5}Ti_2O_7$ samples consolidated by SPS before and after 0.5 dpa He^+ or Kr^{3+} irradiations.

VII.4. Conclusions

Ce-substituted pyrochlore and zirconolite materials consolidated by SPS were subjected to chemical durability and irradiation damage testing. The PCT and MCC-1 were used to test the chemical durability of the samples. Ce release was only detected during the PCT of $CaZr_{0.9}Ce_{0.1}Ti_2O_7$ and $Nd_{1.5}Ce_{0.5}Ti_2O_7$ and the release values were comparable to results of other Ce-substituted materials. During MCC-1 testing (1-49 days), Ce was only released during the 1 and 7 day tests of $Nd_{1.5}Ce_{0.5}Ti_2O_7$. The release value starts out high, and drops dramatically as the test length is increased, as seen in other Ce containing materials. In the MCC-1 testing of other materials and tests longer than 7 days, no Ce was

released above the detectable limit of the ICP-AES. Radiation damage results support the multiphase waste form results. Light ion irradiation had no discernable effect of the structure of the materials according to GIXRD, whereas heavy ion irradiation causes near-complete amorphization of the structure.

VIII. CONCLUSIONS

This thesis focuses on the processing, characterization, and testing of simulated waste forms, both multiphase and single phase, produced by SPS. Sections III and IV detail the multiphase work and they demonstrate the ability of SPS to produce waste forms with desired phase assemblage. Radiation damage studies of these multiphase waste forms show that the smaller grain sizes of SPS produced samples mitigate ion penetration depth. Single phases of zirconolite and pyrochlore were selected for Ce incorporation to simulate actinide and rare earth element immobilization and the work is described in Sections V-VII. Ce incorporation was nearly complete, with only small amounts of perovskite seen in zirconolite materials and both zirconolite and pyrochlore samples exhibit high chemical durability. Detailed summaries are presented in the following sections.

VIII.1. Processing and Radiation Damage of Multiphase Waste Forms

Ceramic compositions targeting a multiphase assemblage were processed using SPS and melt-processing. Both processing routes produced samples with similar phases present, with hollandite as the most predominant phase and perovskite as the other major phase. Zirconium-rich phases were also present in all of the samples and TiO_2 was present in the melt-processed samples. The microstructures of the SPS samples contain small grains (<1μm) of interdispersed phases, while elongated, dendritic grains (>10μm) compose the melt-processed microstructres. Unreacted CeO_2 and Cs-rich phases were obsereved in SPS-processed samples, indicating that further optimization of processing conditions is required.

Radiation damage was simulated in these ceramic waste forms using Au^{3+} and He^{+} ions. When bombarded with heavy ions (Au^{3+}) atomic displacements initiated by ballistic processes caused the affected volumes to amorphize. Similar amorphization behavior was observed in samples produced by both processes when irradiated with Au^{3+} ions, with less ion penetration depth observed in SPS samples which is attributed to the smaller grain sizes of the phases. Exposure to light ions (He^{+}) caused the hollandite phase to break down while the other major phases remained crystalline.

VIII.2. Ce Substitution in Zirconolite and Pyrochlore

Ce incorporation into zirconolite and pyrochlore structures is obtained up to 50 mol% for Zr in the case of zirconolite and 25 mol% for Nd in $Nd_2Ti_2O_7$ pyrochlore using solid state reaction. Small amounts of perovskite (up to 7 wt%) were detected in zirconolite materials with increasing Ce content using XRD. A transition from the 2M polymorph to the 4M polymorph with increasing Ce substitution is seen in zirconolite materials. XANES was used to determine the valence state of Ce in these materials. 2M-zirconolites contain trivalent Ce, which supports Ce substitution on both Ca and Zr sites. Both trivalent and tetravalent Ce was present in 4M-zirconolites. All Ce substituted into pyrochlore materials is converted from tetravalent to trivalent during the reaction process to maintain charge neutrality in the structure.

SPS of Ce-zirconolites causes the 4M-zirconolite polymorph to convert to perovskite and 2M-zirconolite due to the reducing environment inherent to the process. The reduction of Ce^{4+} into Ce^{3+} causes a redistribution of the Ce onto Ca and Zr sites stabilizing the 2M polymorph. A heat treatment in air restores the original phase assemblage. HTXRD was used to study the transformation of the perovskite back into zirconolite. $CaCeTi_2O_7$ forms as an intermediate phase up until 1300°C, and 4M-zirconolite begins at 1350°C. The transformation to 4M-zirconolite is slow, but complete conversion to the original phase assemblage is achieved with a 24h heat treatment in air. The sintering behavior of Ce- substituted pyrochlore is unaffected by Ce content in the material.

VIII.3. Performance Testing of Single Phase Materials

Radiation damage in Ce-substituted zirconolite and pyrochlore was simulated by implanting samples with He^{+} or Au^{3+} with ion fluences equating to 0.5 dpa. GIXRD revealed that light ion (He^{+}) irradiation had very little effect on the materials, whereas heavy ion (Au^{3+}) irradiation caused near complete amorphization of all materials tested. No effect of Ce content on radiation damage behavior was seen. PCT and MCC-1 were used to determine the chemical durability of the Ce containing materials. For zirconolite materials, Ce was only released during the PCT of $CaZr_{0.9}Ce_{0.1}Ti_2O_7$ indicating that the 4M-zirconolite polymorph is more chemically durable than 2M-zirconolite. It was found

that Ce was released from the high Ce content pyrochlore in this study, $Nd_{1.5}Ce_{0.5}Ti_2O_7$, during both the PCT and MCC-1. During MCC-1 tests longer than 7 days, no Ce above the detectable limit of the ICP-AES was released. The Ce release values in these studies were comparable to those in similar tests performed previously.

IX. FUTURE WORK

Multiphase simulated waste forms formed by SPS in this work are comprised of complex phase assemblages and microstructures. Reactive sintering schedules require optimization to improve phase assemblage and eliminate Cs-rich phases. Advanced microscopy (TEM) should be performed on each individual phase after exposure to irradiation to quantify the response of each phase under these conditions. Detailed leaching tests should be paired with microscopy analysis to elucidate the leaching behavior and mechanisms of these multiphase waste forms.

Reactive sintering via SPS of Ce- zirconolite and pyrochlore should be explored in order to simplify and expedite the waste form production process. Supplementary chemical durability and radiation damage experiments to further investigate Ce-substituted zirconolite and pyrochlore behavior under these conditions. For chemical durability tests, Vapor hydration testing (VHT) can be performed to detail the behavior of bulk samples in harsh environments. Leach testing utilizing different leachants will aid in determination of the viability of storage of Ce containing materials.

The 2M- to 4M-zirconolite transition should be further investigated to optimize the Ce loading in zirconolite while maintaining the high chemical durability and resistance to light ion irradiation.

X. REFERENCES

1. G. G. Wicks and D. F. Bickford, “High Level Radioactive Waste - Doing Something About It,” Report DP-1777, Savannah River National Laboratory, Aiken, SC, March 1989.

2. E. Kintisch, "Congress Tells DOE to Take Fresh Look at Recycling Spent Reactor Fuel," *Science,* **310** [5753] 1406 (2005).

3. W. B. Lanham and T. C. Runion, "Purex Process for Plutonium and Uranium Recovery," Report ORNL-479, Oak Ridge National Laboratory, Oak Ridge, TN, October 1949.

4. M. J. Bell, "ORIGEN: The ORNL Isotope Generation and Depletion Code," Report ORNL-4628, Oak Ridge National Laboratory, Oak Ridge, TN, May 1973.

5. International Atomic Energy Agency, "Operational & Long-Term Shutdown Reactors" Accessed on: April 2017. Available at <https://www.iaea.org/PRIS/WorldStatistics/OperationalReactorsByCountry.aspx>

6. Nuclear Energy Institute, “Nuclear Energy Statistics,” Accessed on: April 2017. Available at <https://www.nei.org/Knowledge-Center/Nuclear-Statistics/World-Statistics>

7. International Atomic Energy Agency, "Design and Operation of High Level Waste Vitrification and Storage Facilities," Technical Reports Series No. 339, Vienna, Austria, 1992.

8. L. H. Johnson and D. W. Shoesmith, “Spent Fuel,” pp. 635-98 in *Radioactive Waste Forms for the Future,* Edited by W. Lutze and R. C. Ewing. North- Holland, Amsterdam, 1988.

9. R. Roy, *Radioactive Waste Disposal*. Pergamon, New York, 26-35, 1981.

10. I. W. Donald, B. L. Metcalfe, and R. N. J. Taylor, "The Immobilization of High Level Radioactive Wastes Using Ceramics and Glasses," *J. Mater. Sci.,* **32**, 5851-87 (1997).

11. C. Lopez, X. Deschanels, J. M. Bart, J. M. Boubals, C. Den Auwer, and E. Simoni, "Solubility of Actinide Surrogates in Nuclear Glasses," *J. Nucl. Mater.,* **312** [1] 76-80 (2003).

12. A. Kidari, M. Magnin, R. Caraballo, M. Tribet, F. Doreau, S. Peuget, J.-L. Dussossoy, I. Bardez-Giboire, and C. Jégou, "Solubility and Partitioning of Minor-Actinides and Lanthanides in Alumino-Borosilicate Nuclear Glass," *Procedia Chem.,* **7**, 554-8 (2012).

13. J. N. Cachia, X. Deschanels, C. Den Auwer, O. Pinet, J. Phalippou, C. Hennig, and A. Scheinost, "Enhancing Cerium and Plutonium Solubility by Reduction in Borosilicate Glass," *J. Nucl. Mater.,* **352** [1–3] 182-9 (2006).

14. C. C. Chapman and J. L. Buelt, "Vitrification of High-Level Waste in a Joule-Heated Ceramic Melter," *AlChE Symposium* **75**, 56-60 (1979).

15. B. W. Bowan II, R. Meigs, and E. C. Smith, "Advancements in Joule Heated Melter Technology for Processing U.S. Department of Energy High Level Waste," in *Global 2003: Atoms For Prosperity: Updating Eisenhower's Global Vision for Nuclear Energy: November16-20*, *2003, New Orleans, Louisiana,* American Nuclear Society, La Grange Park, IL, 2003.

16. G. Calas, M. Le Grand, L. Galoisy, and D. Ghaleb, "Structural Role of Molybdenum in Nuclear Glasses: An EXAFS Study," *J. Nucl. Mater.,* **322** [1] 15-20 (2003).

17. O. Pinet, J. L. Dussossoy, C. David, and C. Fillet, "Glass Matrices for Immobilizing Nuclear Waste Containing Molybdenum and Phosphorus," *J. Nucl. Mater.,* **377** [2] 307-12 (2008).

18. R. J. Short, R. J. Hand, and N. C. Hyatt, "Molybdenum in Nuclear Waste Glasses - Incorporation and Redox State," *Mater. Res. Soc. Symp. Proc.,* **757** [II5.4] (2011).

19. S. Gin, A. Abdelouas, L. J. Criscenti, W. L. Ebert, K. Ferrand, T. Geisler, M. T. Harrison, Y. Inagaki, S. Mitsui, K. T. Mueller, J. C. Marra, C. G. Pantano, E. M. Pierce, J. V. Ryan, J. M. Schofield, C. I. Steefel, and J. D. Vienna, "An International Initiative on Long-Term Behavior of High-Level Nuclear Waste Glass," *Mater. Today,* **16** [6] 243-8 (2013).

20. L. J. Liu, J. H. Xu, and Y. Z. Jiang, "Study on Sulfate Phase Segregation and Decomposition in Vitrification Process," *Energy Sci. Technol.,* **49**, 1551-6 (2015).

21. D. Manara, A. Grandjean, O. Pinet, J. L. Dussossoy, and D. R. Neuville, "Sulfur Behavior in Silicate Glasses and Melts: Implications for Sulfate Incorporation in Nuclear Waste Glasses as a Function of Alkali Cation and V_2O_5 Content," *J. Non-Cryst. Solids,* **353** [1] 12-23 (2007).

22. B. C. Sales and L. A. Boatner, "Physical and Chemical Characteristics of Lead-Iron Phosphate Nuclear Waste Glasses," *J. Non-Cryst. Solids,* **79** [1] 83-116 (1986).

23. C. L. Dube, M. C. Stennett, A. S. Gandy, and N. C. Hyatt, "Simulation of Alpha Decay of Actinides in Iron Phosphate Glasses by Ion Irradiation," *Nucl. Instrum. Methods Phys. Res., Sect. B,* **371**, 424-8 (2016).

24. S. T. Reis, D. L. A. Faria, J. R. Martinelli, W. M. Pontuschka, D. E. Day, and C. S. M. Partiti, "Structural Features of Lead Iron Phosphate Glasses," *J. Non-Cryst. Solids,* **304** [1] 188-94 (2002).

25. P. A. Bingham, R. J. Hand, O. M. Hannant, S. D. Forder, and S. H. Kilcoyne, "Effects of Modifier Additions on the Thermal Properties, Chemical Durability, Oxidation State and Structure of Iron Phosphate Glasses," *J. Non-Cryst. Solids,* **355** [28] 1526-38 (2009).

26. B. C. Sales and L. A. Boatner, "Lead-Iron Phosphate Glass: A Stable Storage Medium for High-Level Nuclear Waste," *Science,* **226** [4670] 45 (1984).

27. J. P. Guha, D. Kolar, and B. Volavšek, "Preparation and Characterization of New Ternary Compounds in the System $BaO\text{-}TiO_2\text{-}Al_2O_3$," *J. Solid State Chem.,* **16** [1] 49-54 (1976).

28. W. Sinclair, G. M. McLaughlin, and A. E. Ringwood, "The Structure and Chemistry of a Barium Titanate Hollandite-Type Phase," *Acta Cryst.,* **36** [12] 2913-8 (1980).

29. V. Aubin, D. Caurant, D. Gourier, N. Baffier, T. Advocat, F. Bart, G. Leturcq, and J. M. Costantini, "Synthesis, Characterization and Study of the Radiation Effects on Hollandite Ceramics Developed for Cesium Immobilization," *Mater. Res. Soc. Symp. Proc.,* **807**, 315-20 (2003).

30. W. Sinclair and A. E. Ringwood, "Alpha-Recoil Damage in Natural Zirconolite and Perovskite," *Geochem. J.,* **15** [5] 229-43 (1981).

31. M. Lang, F. Zhang, W. Li, D. Severin, M. Bender, S. Klaumünzer, C. Trautmann, and R. C. Ewing, "Swift Heavy Ion-Induced Amorphization of $CaZrO_3$ Perovskite," *Nucl. Instrum. Methods Phys. Res., Sect. B,* **286**, 271-6 (2012).

32. K. Kuramoto, H. Mitamura, T. Banba, and S. Muraoka, "Development of Ceramic Waste Forms for Actinide-Rich Waste — Radiation Stability of Perovskite and Phase and Chemical Stabilities Of Zr- and Al-Based Ceramics," *Prog. Nucl. Energy,* **32** [3] 509-16 (1998).

33. H. J. Rossell, "Solid Solution of Metal Oxides in the Zirconolite Phase $CaZrTi_2O_7$, II: The Ternary Phase $CaZr_xTi_{3-x}O_7$," *J. Solid State Chem.,* **99**, 52-7 (1992).

34. S. E. Kesson, W. J. Sinclair, and A. E. Ringwood, "Solid Solution Limits in SYNROC Zirconolite," *Nucl. Chem. Waste Man.,* **4**, 259-65 (1983).

35. F. W. Clinard, D. L. Rohr, and R. B. Roof, "Structural Damage in a Self-Irradiated Zirconolite-Based Ceramic," *Nucl. Instrum. Methods Phys. Res., Sect. B*, **1** [2] 581-6 (1984).

36. W. J. Weber, J. W. Wald, and H. Matzke, "Effects of Self-Radiation Damage in Cm-Doped $Gd_2Ti_2O_7$ and $CaZrTi_2O_7$," *J. Nucl. Mater.,* **138** [2] 196-209 (1986).

37. D. M. Strachan, R. D. Scheele, E. C. Buck, J. P. Icenhower, A. E. Kozelisky, R. L. Sell, R. J. Elovich, and W. C. Buchmiller, "Radiation Damage Effects in Candidate Titanates for Pu Disposition: Pyrochlore," *J. Nucl. Mater.,* **345** [2] 109-35 (2005).

38. X. Lu, Y. Ding, H. Dan, M. Wen, X. Mao, Y. Wu, and X. Wang, "High Capacity Immobilization of TRPO Waste by $Gd_2Zr_2O_7$ Pyrochlore," *Mater. Lett.,* **136**, 1-3 (2014).

39. A. Bohre, K. Avasthi, and V. I. Pet'kov, "Vitreous and Crystalline Phosphate High Level Waste Matrices: Present Status and Future Challenges," *J. Ind. Eng. Chem.,,* **50** [Supplement C] 1-14 (2017).

40. J. Choi, W. Um, and S. Choung, "Development of Iron Phosphate Ceramic Waste Form to Immobilize Radioactive Waste Solution," *J. Nucl. Mater.,* **452** [1] 16-23 (2014).

41. V. Pet'kov, E. Asabina, V. Loshkarev, and M. Sukhanov, "Systematic Investigation of The Strontium Zirconium Phosphate Ceramic Form for Nuclear Waste Immobilization," *J. Nucl. Mater.,* **471**, 122-8 (2016).

42. A. E. Ringwood, S. E. Kesson, N. G. Ware, W. Hibberson, and A. Major, "Immobilisation of High Level Nuclear Reactor Wastes in SYNROC," *Nature,* **278**, 219-23 (1979).

43. A. E. Ringwood, V. M. Oversby, S. E. Kesson, W. Sinclair, N. Ware, W. Hibberson, and A. Major, "Immobilization of High-Level Nuclear Reactor Wastes in SYNROC: A Current Appraisal," *Nucl. Chem. Waste Manage.,* **2** [4] 287-305 (1981).

44. A. E. Ringwood, S. E. Kesson, and N. G. Ware, "Immobilization of U.S. Defense Nuclear Wastes Using the SYNROC Process"; pp. 265-72 in *Scientific Basis for Nuclear Waste Management.* Edited by C. J. M. Northrup. Springer US, Boston, MA, 1980.

45. S. E. Kesson and A. E. Ringwood, "Safe Disposal of Spent Nuclear Fuel," *Radioact. Waste Manage. Nucl. Fuel Cycle,* **4** [2] 159-74 (1983).

46. K. L. Smith, G. R. Lumpkin, M. G. Blackford, R. A. Day, and K. P. Hart, "The Durability of SYNROC," *J. Nucl. Mater.,* **190**, 287-94 (1992).

47. A. E. Ringwood, V. M. Oversby, and W. Sinclair, "The Effects of Radiation Damage on SYNROC"; pp. 273-80 in *Scientific Basis for Nuclear Waste Management.* Edited by C. J. M. Northrup. Springer US, Boston, MA, 1980.

48. A. A. Coelho, R. W. Cheary, and K. L. Smith, "Analysis and Structural Determination of Nd-Substituted Zirconolite-4M," *J. Solid State Chem.,* **129** [2] 346-59 (1997).

49. E. R. Vance and D. K. Agrawal, "Incorporation of Radionuclides in Crystalline Titanates," *Nucl. Chem. Waste Manage.,* **3** [4] 229-34 (1982).

50. X. Cai, Y. Teng, L. Wu, K. Zhang, and Y. Huang, "The Synthesis and Chemical Durability of Nd-Doped Single-Phase Zirconolite Solid Solutions," *J. Nucl. Mater.,* **479**, 455-60 (2016).

51. G. Wen, K. Zhang, D. Yin, and H. Zhang, "Solid-State Reaction Synthesis and Aqueous Durability of Ce-Doped Zirconolite-Rich Ceramics," *J. Nucl. Mater.,* **466**, 113-9 (2015).

52. B. M. Clark, S. K. Sundaram, and S. T. Misture, "Polymorphic Transitions in Cerium-Substituted Zirconolite ($CaZrTi_2O_7$)," *Scientific Reports,* **7** [1] 5920 (2017).

53. B. D. Begg and E. R. Vance, "The Incorporation of Cerium in Zirconolite," *Mat. Res. Soc. Symp. Proc.,* **465**, 333-40 (1997).

54. L. A. J. Garvie, H. Xu, Y. Wang, and R. L. Putnam, "Synthesis of $(Ca,Ce^{3+},Ce^{4+})_2Ti_2O_7$: A Pyrochlore with Mixed-Valence Cerium," *J. Phys. Chem. Solids,* **66** [5] 902-5 (2005).

55. S. J. Patwe and A. K. Tyagi, "Solubility of Ce^{4+} and Sr^{2+} in the Pyrochlore Lattice of $Gd_2Zr_2O_7$ for Simulation of Pu and Alkaline Earth Metal," *Ceram. Int.,* **32** [5] 545-8 (2006).

56. K. B. Helean, S. V. Ushakov, C. E. Brown, A. Navrotsky, J. Lian, R. C. Ewing, J. M. Farmer, and L. A. Boatner, "Formation Enthalpies of Rare Earth Titanate Pyrochlores," *J. Solid State Chem.,* **177**, 1858-66 (2004).

57. J. Sloan and R. J. D. Tilley, "Phase Formation in the $Nd_2Ti_2O_7$–$SrTiO_3$ System at 1350°C in the Presence of V_2O_5, CuV_2O_6, or $SrCuO_2$," *J. Solid State Chem.,* **121**, 324-31 (1996).

58. R. C. Ewing, W. J. Weber, and J. Lian, "Nuclear Waste Disposal—Pyrochlore ($A_2B_2O_7$): Nuclear Waste Form for the Immobilization of Plutonium and "Minor" Actinides," *J. Appl. Phys.,* **95** [11] 5949-71 (2004).

59. J. Lian, K. B. Helean, B. J. Kennedy, L. M. Wang, A. Navrotsky, and R. C. Ewing, "Effect of Structure and Thermodynamic Stability on the Response of Lanthanide Stannate Pyrochlores to Ion Beam Irradiation," *J. Phys. Chem. B,* **110** [5] 2343-50 (2006).

60. G. Sattonnay, S. Moll, L. Thomé, C. Legros, A. Calvo, M. Herbst-Ghysel, C. Decorse, and I. Monnet, "Effect of Composition on the Behavior of Pyrochlores Irradiated with Swift Heavy Ions," *Nucl. Instrum. Methods Phys. Res., Sect. B,* **272**, 261-5 (2012).

61. J. Lian, W. J. Weber, W. Jiang, L. M. Wang, L. A. Boatner, and R. C. Ewing, "Radiation-Induced Effects in Pyrochlores and Nanoscale Materials Engineering," *Nucl. Instrum. Methods Phys. Res., Sect. B,* **250** [1–2] 128-36 (2006).

62. M. Lang, F. Zhang, J. Zhang, J. Wang, J. Lian, W. J. Weber, B. Schuster, C. Trautmann, R. Neumann, and R. C. Ewing, "Review of $A_2B_2O_7$ Pyrochlore Response to Irradiation And Pressure," *Nucl. Instrum. Methods Phys. Res., Sect. B,* **268** [19] 2951-9 (2010).

63. U. Brykała, R. Diduszko, K. Jach, and J. Jagielski, "Hot Pressing of Gadolinium Zirconate Pyrochlore," *Ceram. Int.,* **41** [2, Part A] 2015-21 (2015).

64. S. E. Kesson and T. J. White, $[Ba_xCs_y][(Ti,Al)^{3+}_{2x+y}Ti^{4+}_{8-2x-y}]O_{16}$ SYNROC-Type Hollandites. I. Phase Chemistry," *Proc. R. Soc. London, Ser. A,* **405** [1828] 73-101 (1986).

65. V. Aubin-Chevaldonnet, D. Caurant, A. Dannoux, D. Gourier, T. Charpentier, L. Mazerolles, and T. Advocat, "Preparation and Characterization of $(Ba,Cs)(M,Ti)_8O_{16}$ ($M=Al^{3+}$, Fe^{3+}, Ga^{3+}, Cr^{3+}, Sc^{3+}, Mg^{2+}) Hollandite Ceramics Developed for Radioactive Cesium Immobilization," *J. Nucl. Mater.,* **366** [1–2] 137-60 (2007).

66. J. Amoroso, J. Marra, S. D. Conradson, M. Tang, and K. Brinkman, "Melt Processed Single Phase Hollandite Waste Forms For Nuclear Waste Immobilization: $Ba_{1.0}Cs_{0.3}A_{2.3}Ti_{5.7}O_{16}$; A = Cr, Fe, Al," *J. Alloys Compd.,* **584**, 590-9 (2014).

67. R. Cheary, "An Analysis of the Structural Characteristics of Hollandite Compounds," *Acta Cryst.,* **42** [3] 229-36 (1986).

68. R. W. Cheary and J. Kwiatkowska, "An X-ray Structural Analysis of Cesium Substitution in the Barium Hollandite Phase of SYNROC," *J. Nucl. Mater.,* **125** [2] 236-43 (1984).

69. B. Singh, A. A. Rodionov, and Y. L. Khazov, "Nuclear Data Sheets for A = 135," *Nucl. Data Sheets*, **109** [3] 517-698 (2008).

70. A. A. Digeos, J. A. Valdez, K. E. Sickafus, S. Atiq, R. W. Grimes, and A. R. Boccaccini, "Glass Matrix/Pyrochlore Phase Composites for Nuclear Wastes Encapsulation," *J. Mater. Sci.,* **38** [8] 1597-604 (2003).

71. Z. Strnad, "Glass-Ceramic Materials: Liquid Phase Separation, Nucleation and Crystallization in Glasses"; p. 114 in Vol. 8, *Glass Science and Technology.* Elsevier, Amsterdam, 1986.

72. P. Loiseau, D. Caurant, O. Majérus, N. Baffier, and C. Fillet, "Crystallization Study of (TiO_2, ZrO_2)-Rich SiO_2-Al_2O_3-CaO Glasses. Part I Preparation and Characterization of Zirconolite-Based Glass-Ceramics," *J. Mater. Sci.*, **38**, 843-52 2003.

73. E. R. Maddrell, H. C. Paterson, S. E. May, and K. M. Burns, "Phase Evolution in Zirconolite Glass-Ceramic Wasteforms," *J. Nucl. Mater.,* **493**, 380-7 (2017).

74. L. Wu, Y. Li, Y. Teng, and G. Meng, "Preparation and Characterization of Borosilicate Glass-Ceramics Containing Zirconolite and Titanite Crystalline Phases," *J. Non-Cryst. Solids,* **380**, 123-7 (2013).

75. R. Giere, C. T. Williams, and G. R. Lumpkin, "Chemical Characteristics of Natural Zirconolite," *Schweiz. Mineral. Petrogr. Mitt.,* **78**, 433-59 (1998).

76. Y. Deng, Q. Liao, F. Wang, and H. Zhu, "Synthesis and Characterization of Cerium Containing Iron Phosphate Based Glass-Ceramics," *J. Nucl. Mater.,* **499**, 410-8 (2018).

77. H. Li, L. Wu, D. Xu, X. Wang, Y. Teng, and Y. Li, "Structure and Chemical Durability of Barium Borosilicate Glass–Ceramics Containing Zirconolite and Titanite Crystalline Phases," *J. Nucl. Mater.,* **466**, 484-90 (2015).

78. E. Paknahad and A. P. Grosvenor, "Investigation of the Stability of Glass-Ceramic Composites Containing $CeTi_2O_6$ and $CaZrTi_2O_7$ After Ion Implantation," *Solid State Sciences,* **74**, 109-17 (2017).

79. M. Tang, A. Kossoy, G. Jarvinen, J. Crum, L. Turo, B. Riley, K. Brinkman, K. Fox, J. Amoroso, and J. Marra, "Radiation Stability Test on Multiphase Glass Ceramic and Crystalline Ceramic Waste Forms," *Nucl. Instrum. Methods Phys. Res., Sect. B,* **326**, 293-7 (2014).

80. J. Y. Lee, D. K. Cho, H. J. Choi, J. W. Choi, and L. M. Wang, "Analyses of Disposal Efficiency Based on Nuclear Spent Fuel Cooling Time and Disposal Tunnel/Pit Spacing for the Design of a Geological Repository," *Prog. Nucl. Energy,* **53** [4] 361-7 (2011).

81. E. R. Vance, B. D. Begg, and D. J. Gregg, "Immobilization of High-Level Radioactive Waste and Used Nuclear Fuel for Safe Disposal in Geological Repository Systems"; pp. 269-95 in *Geological Repository Systems for Safe Disposal of Spent Nuclear Fuels and Radioactive Waste (2nd ed.).* Woodhead Publishing, Sawston, UK, 2017.

82. B. Grambow, C. Landesman, and S. Ribet, "Nuclear Waste Disposal: I. Laboratory Simulation of Repository Properties," *Appl. Geochem.,* **49** [Supplement C] 237-46 (2014).

83. B. W. Arnold, P. V. Brady, S. J. Bauer, C. Herrick, S. Pye, and J. Finger, "Reference Design and Operations for Deep Borehole Disposal of High-Level Radioactive Waste," SAND2011-6749, Sandia National Laboratry, Albuquerque, NM, October 2011.

84. B. W. Arnold, P. V. Brady, S. Altman, P. Vaughn, D. Nielson, J. Lee, F. Gibb, P. Mariner, K. Travis, W. Halsey, J. Beswick, and J. Tillman, "Deep Borehole Disposal Research: Demonstration Site Selection Guidelines, Borehole Seals Design, and RD&D Needs," SAND2013-9490P, Sandia National Laboratory, Albuquerque, NM, October 2013.

85. J. Beswick, "Status of Technology for Deep Borehole Disposal," Contract No NP 01185, EPS International, Houston, TX, April 2008.

86. M. Nygren and Z. Shen, "Hot Pressing and Spark Plasma Sintering"; pp. 189-214 in *Ceramics Science and Technology* Vol. 3 Synthesis and Processing. Edited by R. Riedel and I.-W. Chen. Wiley-VCH Verlag GmbH &Co., Weinheim, DE, 2012.

87. J. Amoroso, J. C. Marra, M. Tang, Y. Lin, F. Chen, D. Su, and K. S. Brinkman, "Melt Processed Multiphase Ceramic Waste Forms for Nuclear Waste Immobilization," *J. Nucl. Mater.,* **454** [1] 12-21 (2014).

88. P. Tumurugoti, S. Sundaram, K. Brinkman, J. Amoroso, and K. Fox, "Melt-Processed Multiphasic Ceramic Waste Forms," *Ceram. Trans.,* **250**, 205-12 (2014).

89. E. Vernaz, S. Gin, and C. Veyer, "5.18 - Waste Glass"; pp. 451-83 in *Comprehensive Nuclear Materials.* Edited by R. J. M. Konings. Elsevier, Oxford, UK, 2012.

90. M. L. Carter, M. W. A. Stewart, S. H. F. Leung, and M. Colella, “Microstructures of Inactive SYNROC-C Samples Produced by Different Hot-Consolidation Method,” *Ceram. Trans.,* **71**, 491-504 (1996).

91. A. E. Osmanlioglu, "Immobilization of Radioactive Waste by Cementation With Purified Kaolin Clay," *Waste Manage.,* **22**, 481-3 (2002).

92. T. Murakami, "Microstructure of SYNROC," *Chem. Waste Man.,* **5**, 269-78 (1985).

93. G. R. Lumpkin, K. L. Smith, and M. G. Blackford, "Partitioning of Uranium and Rare Earth Elements in SYNROC: Effect of Impurities, Metal Additive, and Waste Loading," *J. Nucl. Mater.,* **224**, 31-42 (1995).

94. S. X. Wang, G. R. Lumpkin, L. M. Wang, and R. C. Ewing, "Ion Irradiation-Induced Amorphization of Six Zirconolite Compositions," *Nucl. Instrum. Methods Phys. Res., Sect. B,* **166–167**, 293-8 (2000).

95. V. Picot, X. Deschanels, S. Peuget, B. Glorieux, A. M. Seydoux-Guillaume, and R. Wirth, "Ion Beam Radiation Effects in Monazite," *J. Nucl. Mater.,* **381** [3] 290-6 (2008).

96. W. J. Weber, R. C. Ewing, C. R. A. Catlow, T. D. Rubia, L. W. Hobbs, C. Kinoshita, H. Matzke, A. T. Motta, M. Nastasi, E. K. H. Salje, E. R. Vance, and S. J. Zinkle, "Radiation Effects in Crystalline Ceramics for the Immobilization of High-Level Nuclear Waste and Plutonium," *J. Mater. Res.,* **13**, 1434-84 (1998).

97. C. Davoisne, M. C. Stennett, N. C. Hyatt, N. Peng, C. Jeynes, and W. E. Lee, "Krypton Irradiation Damage in Nd-Doped Zirconolite and Perovskite," *J. Nucl. Mater.,* **415** [1] 67-73 (2011).

98. J. Lian, L. M. Wang, R. C. Ewing, and L. A. Boatner, "Ion Beam Implantation and Cross-Sectional TEM Studies of Lanthanide Titanate Pyrochlore Single Crystals," *Nucl. Instrum. Methods Phys. Res., Sect. B,* **241** [1–4] 365-71 (2005).

99. S. X. Wang, L. M. Wang, R. C. Ewing, G. S. Was, and G. R. Lumpkin, "Ion Irradiation-Induced Phase Transformation of Pyrochlore And Zirconolite," *Nucl. Instrum. Methods Phys. Res., Sect. B,* **148** [1–4] 704-9 (1999).

100. Y. Zhang, J. Jagielski, I.-T. Bae, X. Xiang, L. Thomé, G. Balakrishnan, D. M. Paul, and W. J. Weber, "Damage Evolution in Au-Implanted $Ho_2Ti_2O_7$ Titanate Pyrochlore," *Nucl. Instrum. Methods Phys. Res., Sect. B,* **268** [19] 3009-13 (2010).

101. K. E. Sickafus, R. W. Grimes, J. A. Valdez, A. Cleave, M. Tang, M. Ishimaru, S. M. Corish, C. R. Stanek, and B. P. Uberuaga, "Radiation-Induced Amorphization Resistance and Radiation Tolerance in Structurally Related Oxides," *Nat. Mater.,* **6** [3] 217-23 (2007).

102. J. D. Vienna, E. D. Collins, J. V. Crum, W. L. Ebert, S. M. Frank, T. G. Gam, D. Gombert, R. Jones, R. T. Jubin, V. C. Maio, J. C. Marra, J. Matyas, T. M. Nenoff, B. J. Riley, G. J. Sevigny, N. R. Soelberg, D. M. Strachan, P. K. Thallapally, and J. H. Westsik, "Closed Fuel Cycle Waste Treatment Strategy, Fuel Cycle Research & Development," PNNL-24114, Idaho National Laboratory, Idaho Falls, ID, February 2014.

103. S. E. Kesson and C. J. Ball, "A Review of Radiation Effects in SYNROC and Related Titanate Phases," *J. Aust. Ceram. Soc.,* **24** [1] 89-99 (1988).

104. D. Men, M. K. Patel, I. O. Usov, M. Toiammou, I. Monnet, J. C. Pivin, J. R. Porter, and M. L. Mecartney, "Radiation Damage in Multiphase Ceramics," *J. Nucl. Mater.,* **443** [1] 120-7 (2013).

105. S. Thevuthasan, C. H. F. Peden, M. H. Engelhard, D. R. Baer, G. S. Herman, W. Jiang, Y. Liang, and W. J. Weber, "The Ion Beam Materials Analysis Laboratory at the Environmental Molecular Sciences Laboratory," *Nucl. Instrum. Methods Phys. Res.,Sect. A,* **420** [1–2] 81-9 (1999).

106. R. C. Ewing, W. J. Weber, and F. W. Clinard, "Radiation Effects in Nuclear Waste Forms for High-Level Radioactive Waste," *Prog. Nucl. Energy,* **29**, 63-127 (1995).

107. J. F. Ziegler, J. P. Biersack, and U. Littmark, *The Stopping and Range of Ions in Matter*. Pergamon Press, New York, 1985.

108. M. Tang, P. Tumurugoti, B. Clark, S. K. Sundaram, J. Amoroso, J. Marra, C. Sun, P. Lu, Y. Wang, and Y. B. Jiang, "Heavy Ion Irradiations on Synthetic Hollandite-Type Materials: $Ba_{1.0}Cs_{0.3}A_{2.3}Ti_{5.7}O_{16}$ (A=Cr, Fe, Al)," *J. Solid State Chem.,* **239**, 58-63 (2016).

109. T. D. Shen, "Radiation Tolerance in a Nanostructure: Is Smaller Better?," *Nucl. Instrum. Methods Phys. Res., Sect. B,* **266** [6] 921-5 (2008).

110. K. Jin, Y. Zhang, H. Xue, Z. Zhu, and W. J. Weber, "Ion Distribution and Electronic Stopping Power for Au Ions in Silicon Carbide," *Nucl. Instrum. Methods Phys. Res., Sect. B,* **307**, 65-70 (2013).

111. G. Grzinic, L. A. Bursill, and D. J. Smith, "The Hollandite-Related Structure of $Ba_2Ti_9O_{20}$," *J. Solid State Chem.,* **47** [2] 151-63 (1983).

112. G. D. Fallon and B. M. Gatehouse, "The Crystal Structure of $Ba_2Ti_9O_{20}$: A Hollandite Related Compound," *J. Solid State Chem.,* **49** [1] 59-64 (1983).

113. I. W. Donald, *Waste Immobilization in Glass and Ceramic Based Hosts: Radioactive, Toxic and Hazardous Wastes,* 1st ed. Wiley, West Sussex. UK, 2010.

114. C. W. Bjorklund, "The Preparation of PuP_2O_7 and $PuPO_4$," *J. Am. Chem. Soc.,* **79** [24] 6347-50 (1957).

115. J. C. Marra, A. D. Cozzi, R. A. Pierce, J. M. Pareiza, A. R. Jurgensen, and D. M. Missimer, "Cerium as a Surrogate in the Plutonium Immobilized Form," WSRC-MS-2001-00007, Savannah River National Laboratory, Aiken, SC, June 2001.

116. M. V. Zamoryanskaya and B. E. Burakov, "Feasabilty Limits in Using Cerium as a Surrogate for Plutonium Incorporation in Zircon, Zirconia And Pyrochlore," *Mat. Res. Soc. Symp. Proc.,* **663**, 301-6 (2000).

117. E. R. Vance, B. D. Begg, R. A. Day, and C. J. Ball, "Zirconolite-Rich Ceramics for Actinide Wastes," *Mater. Res. Soc. Symp. Proc.,* **353**, 767-74 (1994).

118. X. J. Wang, H. Y. Xiao, X. T. Zu, and W. J. Weber, "Study of Cerium Solubility in $Gd_2Zr_2O_7$ by DFT + U Calculations," *J. Nucl. Mater.,* **419** [1–3] 105-11 (2011).

119. C. G. Liu, D. Y. Yang, L. J. Chen, H. Liu, Y. Xia, J. Wen, L. Y. Dong, K. Q. Zhang, A. Z. Xiang, and Y. H. Li, "The Solubility of Cerium in $La_2Ti_2O_7$ by DFT + U Calculations," *J. Alloys Compd.,* **648**, 609-14 (2015).

120. X. J. Wang, H. Y. Xiao, X. T. Zu, and W. J. Weber, "A DFT + U Study of Cerium Solubility in $La_2Zr_2O_7$," *J. Nucl. Mater.,* **424** [1–3] 69-74 (2012).

121. B. Mandal and A. Tyagi, "Pyrochlores: Potential Multifunctional Materials," *BARC Newsletter,* [313] 6-13 (2010).

122. Y. Teng, S. Wang, Y. Huang, and K. Zhang, "Low-Temperature Reactive Hot-Pressing of Cerium-Doped Titanate Composite Ceramics and Their Aqueous Stability," *J. Eur. Ceram. Soc.,* **34** [4] 985-90 (2014).

123. M. Pirzada, R. W. Grimes, L. Minervini, J. F. Maguire, and K. E. Sickafus, "Oxygen Migration in $A_2B_2O_7$ pyrochlores," *Solid State Ionics,* **140**, 201-8 (2001).

124. L. Minervini, R. W. Grimes, Y. Tabira, R. L. Withers, and K. E. Sickafus, "The Oxygen Positional Parameter in Pyrochlores and Its Dependece on Disorder," *Phil. Mag. A,* **82**, 123-35 (2002).

125. P. J. Wilde and C. R. A. Catlow, "Defects and Diffusion in Pyrochlore Structured Oxides," *Solid State Ionics,* **112**, 173-83 (1998).

126. J. D. Gale, "General Utility Lattice Program Manual," Version 3.4, Nanochemistry Research Institute, Department of Chemistry,Curtin University, Perth, AUS, 2003.

127. N. F. Mott and M. J. Littleton, "Conduction in Polar Crystals. I. Electrolytic Conduction in Solid Salts," *Trans. Faraday Soc.,* **34**, 485-99 (1938).

128. S. T. Misture, "Large-Volume Atmosphere-Controlled High-Temperature X-ray Diffraction Furnace," *Meas. Sci. Technol.,* **14** [7] 1091-8 (2003).

129. N. Ishizawa, K. Ninomiya, T. Sakakura, and J. Wang, "Redetermination of $Nd_2Ti_2O_7$: A Non-Centrosymmetric Structure with Perovskite-Type Slabs," *Acta Cryst,,* **E69 [**i19] (2013).

130. X. Deschanels, A. M. Seydoux-Guillaume, V. Magnin, A. Mesbah, M. Tribet, M. P. Moloney, Y. Serruys, and S. Peuget, "Swelling Induced by Alpha Decay in Monazite and Zirconolite Ceramics: A XRD and TEM Comparative Study," *J. Nucl. Mater.,* **448** [1–3] 184-94 (2014).

131. B. D. Begg, E. R. Vance, B. A. Hunter, and J. V. Hanna, "Zirconolite Transformation Under Reducing Conditions," *J. Mater. Res.,* **13** [11] 3181-90 (1998).

132. R. Chaim, A. Shlayer, and C. Estournes, "Densification of Nanocrystalline Y_2O_3 Ceramic Powder by Spark Plasma Sintering," *J. Eur. Ceram. Soc.,* **29**, 91-8 (2009).

133. Z. Shen, M. Johnsson, Z. Zhao, and M. Nygren, "Spark Plasma Sintering of Alumina," *J. Am. Ceram. Soc.,* **85**, 1921-7 (2002).

134. Y. J. Wu, J. Li, X. M. Chen, and K. Kakegawa, "Densification and Microstructures of $PbTiO_3$ Ceramics Prepared by Spark Plasma Sintering," *J. Mater. Sci. Eng. A,* **527**, 5157-60 (2010).

135. S. Nowak, L. Perriere, L. Dembinski, S. Tusseau-Nenez, and Y. Champion, "Approach of the Spark Plasma Sintering Mechanism in $Zr_{57}Cu_{20}Al_{10}Ni_8Ti_5$ Metallic Glass," *J. Alloy. Compd.,* **509**, 1011-9 (2011).

136. S. Jieguang, L. Junguo, S. Jianrong, and Z. Lianmeng, "Mechanism of Sintering YAG/ZrB_2 Multiphase Ceramics with Spark Plasma Sintering," *Mater. Manuf. Processes,* **23** [5] 475-8 (2008).

137. J. G. Santanach, A. Weibel, C. Estournes, Q. Yang, C. Laurent, and A. Peigney, "Spark Plasma Sintering of Alumina: Study of Parameters, Formal Sintering Analysis and Hypotheses on the Mechanism(s) Involved in Densification and Grain Growth," *Acta Mater.,* **59**, 1400-8 (2011).

138. R. Chaim, "Densification Mechanisms in Spark Plasma Sintering of Nanocrystalline Ceramics," *J. Mater. Sci. Eng. A,* **443**, 25-32 (2007).

139. G. Bernard-Granger, A. Néri, C. Navone, M. Soulier, J. Simon, and M. Marinova-Atanassova, "Spark Plasma Sintering of a p-type $Si_{1-x}Ge_x$ Alloy: Identification of the Densification Mechanism by Isothermal and Anisothermal Methods," *J. Mater. Sci.,* **47** [10] 4313-25 (2012).

140. G. Bernard-Granger and C. Guizard, "Spark Plasma Sintering of a Commercially Available Granulated Zirconia Powder: I. Sintering Path and Hypotheses About the Mechanism(s) Controlling Densification," *Acta Mater.,* **55** [10] 3493-504 (2007).

141. P. Guyot, G. Antou, N. Pradeilles, A. Weibel, M. Vandenhende, G. Chevallier, A. Peigney, C. Estournès, and A. Maître, "Hot Pressing and Spark Plasma Sintering of Alumina: Discussion About an Analytical Modelling Used for Sintering Mechanism Determination," *Scr. Mater.,* **84–85**, 35-8 (2014).

142. D. Chakravarty and A. H. Chokshi, "Direct Characterizing of Densification Mechanisms During Spark Plasma Sintering," *J. Am. Ceram. Soc.,* **97** [3] 765-71 (2014).

143. M. N. Rahaman, " Theory of Solid-State and Viscous Sintering"; p. 521 in *Ceramic Processing and Sintering,* Marcel Dekker, New York, 2003.

144. G. Antou, N. Pradeilles, M. Gendre, and A. Maître, "New Approach of the Evolution of Densification Mechanisms During Spark Plasma Sintering: Application to Zirconium (Oxy-)Carbide Ceramics," *Scr. Mater.,* **101**, 103-6 (2015).

145. G. Antou, P. Guyot, N. Pradeilles, M. Vandenhende, and A. Maître, "Identification of Densification Mechanisms of Pressure-Assisted Sintering: Application to Hot Pressing and Spark Plasma Sintering of Alumina," *J. Mater. Sci.,* **50** [5] 2327-36 (2015).

146. "Standard Test Methods for Determining Average Grain Size," ASTM Designation E112-13. American Society for Testing and Materials, West Conshohocken, PA.

147. T. G. Langdon, "Grain Boundary Sliding as a Deformation Mechanism During Creep," *Philos. Mag.,* **22** [178] 689-700 (1970).

148. B.-N. Kim, K. Hiraga, S. Grasso, K. Morita, H. Yoshida, H. Zhang, and Y. Sakka, "High-Pressure Spark Plasma Sintering of MgO-Doped Transparent Alumina," *J. Ceram. Soc. Jpn.,* **120** [1399] 116-8 (2012).

149. S. R. Bakshi, V. Musaramthota, D. Lahiri, V. Singh, S. Seal, and A. Agarwal, "Spark Plasma Sintered Tantalum Carbide: Effect of Pressure and Nano-Boron Carbide Addition on Microstructure and Mechanical Properties," *J. Mater. Sci. Eng. A,* **528** [3] 1287-95 (2011).

150. R. L. Coble, "A Model for Boundary Diffusion Controlled Creep in Polycrystalline Materials," *J. Appl. Phys.,* **34** [6] 1679-82 (1963).

151. "Standard Test Methods for Determining Chemical Durability of Nuclear, Hazardous, and Mixed Waste Glasses and Multiphase Glass Ceramics: The Product Consistency Test (PCT)," ASTM Designation C1285-14. American Society for Testing and Materials, West Conshohocken, PA.

152. K. Brinkman, K. Fox, J. Marra, J. Reppert, J. Crum, and M. Tang, "Single Phase Melt Processed Powellite (Ba,Ca)MoO_4 for the Immobilization of Mo-Rich Nuclear Waste," *J. Alloys Compd.,* **551**, 136-42 (2013).

153. D. M. Strachan, "Results From Long-Term Use of the MCC-1 Static Leach Test Method," *Nucl. Chem. Waste Manage.,* **4** [2] 177-88 (1983).

154. S. V. Stefanovsky, S. V. Yudintsev, S. A. Perevalov, I. V. Startseva, and G. A. Varlakova, "Leach Resistance of Murataite-Based Ceramics Containing Actinides," *J. Alloys Compd.,* **444–445**, 618-20 (2007).

155. "Standard Test Method for Measuring Waste Glass or Glass Ceramic Durability by Vapor Hydration Test," ASTM Designation C1663-09. American Society for Testing and Materials, West Conshohocken, PA.

156. C. Martin, I. Ribet, P. Frugier, and S. Gin, "Alteration Kinetics of the Glass-Ceramic Zirconolite and Role of the Alteration Film – Comparison with the SON68 Glass," *J. Nucl. Mater.,* **366** [1–2] 277-87 (2007).

157. W. L. Gong, L. M. Wang, R. C. Ewing, E. Vernaz, J. K. Bates, and W. L. Ebert, "Analytical Electron Microscopy Study of Surface Layers Formed on the French SON68 Nuclear Waste Glass During Vapor Hydration at 200°C," *J. Nucl. Mater.,* **254** [2–3] 249-65 (1998).

158. G. Leturcq, P. J. McGlinn, C. Barbe, M. G. Blackford, and K. S. Finnie, "Aqueous Alteration of Nearly Pure Nd-Doped Zirconolite ($Ca_{0.8}Nd_{0.2}ZrTi_{1.8}Al_{0.2}O_7$), A Passivating Layer Control," *Appl. Geochem.,* **20**, 899-906 (2005).

159. P. Pöml, T. Geisler, J. Cobos-Sabaté, T. Wiss, P. E. Raison, P. Schmid-Beurmann, X. Deschanels, C. Jégou, J. Heimink, and A. Putnis, "The Mechanism of the Hydrothermal Alteration of Cerium- and Plutonium-Doped Zirconolite," *J. Nucl. Mater.,* **410** [1] 10-23 (2011).

160. G. R. Lumpkin, "Alpha-Decay Damage and Aqueous Durability of Actinide Host Phases in Natural Systems," *J. Nucl. Mater.,* **289** [1] 136-66 (2001).

161. D. Yin, K. Zhang, L. Peng, Z. He, Y. Liu, H. Zhang, and X. Lu, "Solid-State Reaction Synthesis and Chemical Stability Studies in Nd-Doped Zirconolite-Rich Ceramics," *J. Rare Earths,* **36** [5] 492-8 (2018).

162. L. Fan, X. Shu, X. Lu, Y. Xie, Y. Ding, T. Duan, B. Dang, and Y. Wu, "Phase Structure and Aqueous Stability of TRPO Waste Incorporation into $Gd_2Zr_2O_7$ Pyrochlore," *Ceram. Int.,* **41** [9, Part B] 11741-7 (2015).

163. P. Pöml, M. Menneken, T. Stephan, D. R. D. Niedermeier, T. Geisler, and A. Putnis, "Mechanism of Hydrothermal Alteration of Natural Self-Irradiated And Synthetic Crystalline Titanate-Based Pyrochlore," *Geochim. Cosmochim. Acta,* **71** [13] 3311-22 (2007).

164. L. Peng, K. Zhang, D. Yin, J. Wu, S. He, and H. He, "Self-Propagating Synthesis, Mechanical Property and Aqueous Durability of $Gd_2Ti_2O_7$ Pyrochlore," *Ceram. Int.,* **42** [16] 18907-13 (2016).

165. X. Lu, L. Fan, X. Shu, S. Su, Y. Ding, and F. Yi, "Phase Evolution and Chemical Durability of Co-Doped $Gd_2Zr_2O_7$ Ceramics for Nuclear Waste Forms," *Ceram. Int.,* **41** [5, Part A] 6344-9 (2015).

166. X. Lu, X. Shu, S. Chen, K. Zhang, F. Chi, H. Zhang, D. Shao, and X. Mao, "Heavy-Ion Irradiation Effects on U_3O_8 Incorporated $Gd_2Zr_2O_7$ Waste Forms," *J. Hazard. Mater.,* **357**, 424-30 (2018).

167. M. Gupta, P. K. Kulriya, R. Shukla, R. S. Dhaka, R. Kumar, and S. S. Ghumman, "Reduction and Structural Modification of Zirconolite on He^+ Ion Irradiation," *Nucl. Instrum. Methods Phys. Res., Sect. B,* **379**, 119-25 (2016).

168. R. C. Ewing and L. M. Wang, "Amorphization of Zirconolite: Alpha-Decay Event Damage Versus Krypton Ion Irradiation," *Nucl. Instrum. Methods Phys. Res., Sect. B,* **65** [1] 319-23 (1992).

169. K. L. Smith, N. J. Zaluzec, and G. R. Lumpkin, "In Situ Studies of Ion Irradiated Zirconolite, Pyrochlore and Perovskite," *J. Nucl. Mater.,* **250** [1] 36-52 (1997).

170. D. M. Strachan, R. P. Turcotte, and B. O. Barnes, "MCC-1: A Standard Leach Test for Nuclear Waste Forms," *Nucl. Technol.,* **56**, 306-9 (1982).

171. Y. Ding, X. Long, S. Peng, D. Zhang, Z. Tan, and X. Lu, "Phase Evolution and Aqueous Durability of $Zr_{1-x-y}Ce_xNd_yO_{2-y/2}$ Ceramics Designed to Immobilize Actinides with Multi-Valences," *J. Nucl. Mater.,* **487**, 297-304 (2017).

172. J. Wang, J. Wang, Y. Zhang, Y. Li, Y. Teng, Z. Wang, and H. Tan, "Flux Synthesis and Chemical Stability of Nd and Ce Co-Doped $(Gd_{1-X}Nd_x)_2(Zr_{1-X}Ce_x)_2O_7$ ($0 \leq X \leq 1$) Pyrochlore Ceramics for Nuclear Waste Forms," *Ceram. Int.,* **43** [18] 17064-70 (2017).